In-situ growth of C-F@CCS@ZIF8/67–1/1 photocatalysts with internal electric field and interfacial enhancement on cobalt-copper foam surface for simultaneous removal of ciprofloxacin and Cr(VI)

Jiliang Niu [a], Ruixiang Hu [a], Liwen Tang [a], Yuxin Huang [a], Jianhua Cheng [a,b,*], Yongyou Hu [a]

[a] *Ministry of Education Key Laboratory of Pollution Control and Ecological Remediation for Industrial Agglomeration Area, College of Environment and Energy, South China University of Technology, Guangzhou 510006, China*
[b] *South China Institute of Collaborative Innovation, Dongguan 523808, China*

ARTICLE INFO

ABSTRACT

ZIF8/67–1/1 and CuCo$_2$S$_4$ were grown on the surface of cobalt-copper foam by in-situ growth method, and p-n heterostructures were formed by induction of internal electric field. The DFT calculation reveals that the energy levels near the Fermi level are gradually distributed continuously after ZIF8/67–1/1 and CuCo$_2$S$_4$ recombination, which accelerates electron conduction. Furthermore, the electron orbitals in the composite structure are real-located and the electrical conductivity of the interface is improved. This strong interfacial enhancement promotes the transfer of photoexcited electrons and promotes the photoinduced separation of electron-hole pairs. Thanks to the surface oxygen vacancy and unique structure, C-F@CCS@ZIF8/67–1/1 composites can simultaneously achieve 97.2% ciprofloxacin (CIP) degradation and 96.5% Cr(VI) reduction. This catalyst does not require any recycling process and remains structurally stable during use with only a minimal amount of metal leaching. This work also reveals the mechanism of heterojunction formation between metal-organic frameworks and sulfides, broadening their application potential.

1. Introduction

The compound environmental pollution caused by various organic pollutants and heavy metals in wastewater has seriously hindered the sustainable development of human society [1]. Among organic pollutants, antibiotics have become a hot research topic due to the problems of difficult degradation, persistent toxicity and bacterial resistance. Thanks to its broad-spectrum antibacterial activity and good bactericidal effect, CIP, as a third-generation quinolone antibiotic, is widely used in all aspects of human medicine, animal husbandry and agriculture [2]. In addition, Cr(VI) is considered to be one of the most toxic heavy metal ions [3]. Chromium-based materials have been widely used in many industrial applications, such as electroplating, metallurgy, film and television, leather tanning, refractory manufacturing and ceramic colorants. Of the two typical oxidation states of Cr in water-based media, Cr (III) is far less harmful than Cr(VI), and Cr(VI) is more difficult to physically and chemically remove from water than Cr(III) [4]. The unreasonable discharge of industrial and agricultural wastewater and the

cross-enrichment of the natural circulation systems have resulted in the coexistence of Cr(VI) and CIP in wastewater. At present, a series of technologies have been developed to remove antibiotics and Cr(VI), such as the adsorption method, chemical precipitation method, biodegradation, etc. [5,6]. However, these traditional methods to remove such complex pollutants are very inefficient and easy to cause secondary pollution. Photocatalysis technology has attracted extensive attention in recent years due to its advantages of environmental friendliness, wide sources and sustainable development [7,8].

Semiconductor photocatalysis is an effective way to solve environmental problems, so various photocatalysts have been widely studied for environmental treatment and remediation [9]. However, the traditional application of photocatalyst is limited by three problems: i) Recovery and secondary pollution caused by powder state; ii) Photogenerated carriers are easy to recombine and cannot drive the subsequent REDOX reaction; iii) Wide band gaps cannot be excited in visible or solar light (photons from the sun can stimulate semiconductors with narrow band gaps < 3.0 eV) [10–12]. Therefore, it is very challenging and desirable to

explore special photocatalysts with excellent visible light absorption (about 43% of solar energy) and charge separation capabilities for practical photocatalytic applications [13,14]. The construction of heterojunction by depositing or growing the active component on the surface of the recyclable substrate is considered to be a relatively effective measure, which can not only improve the charge transfer efficiency but also provide more active sites for photocatalytic reactions. Unfortunately, during the preparation process, agglomeration often occurs between the different active components, which seriously affects the contact area between the photocatalyst and the contaminants. Moreover, the traditional surface load structure is unstable and easy to dissolve, resulting in secondary pollution [15,16].

Fortunately, metal foams with three-dimensional porous structures, such as cobalt-copper foams (C-F), have become promising recyclable substrates [17]. C-F has a large surface area, excellent electrical conductivity, reasonable price, mechanical stability and plasticity structure, and elevated metal activity on the surface is easy to induce in situ reaction. Zeolite imidazolate frameworks (ZIFs) are a new zeolite material with a regular porous nanocage structure, belonging to metal-organic frames (MOFs) [18]. Among them, ZIF8 and 67 have high thermal and hydrothermal stability, high porosity, and large specific surface area, which is conducive to the adsorption of pollutant molecules and provides additional oxidation reaction centers [19]. In addition, the imidazole group in ZIF8 and 67 has abundant π electron dissociation, providing electrons for metal nanoparticles as electron donors, promoting the interfacial electron conversion rate, thus improving the catalytic efficiency. Bimetallic sulfur spinel $CuCo_2S_4$ is a valuable photocatalyst [20]. On the one hand, sulfur is less electronegative, which makes it have higher conductivity. On the other hand, the material has a narrow band gap of 1.5–2.5 eV, which can absorb visible light and be used in photocatalytic reactions. Although the above materials have relatively excellent photocatalytic performance, there are few reports on how to construct recyclable heterojunction materials on the surface of metal foam. The main reason is that the oxidation of metal atoms on the surface of metal foam is uncontrollable, non-selective and greatly active. In recent years, a variety of heterojunction photocatalysts based on ZIFs or sulfide have been developed and shown excellent photocatalytic efficiency. However, the mechanism of enhancing photocatalytic activity based on the electron band structure of ZIFs and sulfide heterojunction remains unclear and needs to be further elucidated [21].

Herein, we successfully grew $CuCo_2S_4$ vertical nanosheets in situ on the surface of C-F and anchored ZIF8/67–1/1 nanoparticles on the surface of $CuCo_2S_4$ to further cooperate with each other to form p-n heterojunction, achieving synchronous removal of CIP and Cr(VI) in wastewater. The mechanism of its excellent photocatalytic activity was investigated. Through DFT calculation and experiment, it is found that the enhanced interface effect of $CuCo_2S_4$ and ZIF8/67–1/1 improves the electron transfer efficiency and induces the internal electric field to accelerate the light-induced charge transfer. In addition, surface oxygen vacancies and synergistic effects can promote the rate of electron-hole separation and free radical production. C-F@CCS@ZIF8/67–1/1 is insitu grown on the surface of C-F and the formed heterojunction is close, which can achieve maintaining structural stability in complex water. At the same time, no recovery operation is required during use and no secondary pollution is generated. According to the results of the LC-MS test, the possible degradation pathway of CIP was proposed, and the toxicity of the generated intermediate was predicted and evaluated by quantitative structure-activity relationship (QSAR). The above research shows that the prepared C-F@CCS@ZIF8/67–1/1 composite photocatalyst has great potential in treating the actual composite polluted wastewater.

2. Experimental procedure

2.1. Catalyst preparation

2.1.1. Synthesis of C-F@ZIF

A variety of composite photocatalysts were prepared by simple vulcanization reaction and in-situ synthesis, as shown in Scheme 1. Firstly, a piece of cobalt-copper foam (C-F, 1 cm in diameter and 1.5 mm thick) was ultrasonically cleaned with dilute hydrochloric acid, ethanol and deionized water, respectively. The cleaned C-F was added into 60 mL methanol solution containing $Zn(NO_3)_3 \cdot 6 H_2O$ (6.0, 4.0, 3.0, 2.0 or 0 mmol) and $Co(NO_3)_3 \cdot 6 H_2O$ (0.0, 2.0, 3.0, 4.0 or 6.0 mmol) at the same time. Then 3.0 mmol of dimethylimidazole was added and stirred well. The mixed solution was reflowed for 2 h at 60 ℃, that is, C-F@ZIF samples with different load ratios were obtained. They are named as C-F@ZIF8, C-F@ZIF8/67–2/1, C-F@ZIF8/67–1/1, C-F@ZIF8/67–1/2 and C-F@ZIF67 respectively.

2.1.2. Synthesis of C-F@CuCo₂S₄

After cleaning C-F according to the above steps, it was put into the tube furnace together with the porcelain ark containing 0.5 g settling sulfur powder. The C-F@CuCo₂S₄ grown in situ on the surface of C-F was obtained by holding the ark at 180 ℃ under an argon atmosphere for 20 h.

#### 2.1.3. Synthesis of C-F@CuCo₂S₄ @ZIF

The C-F@CuCo₂S₄ obtained from the above steps was simultaneously added to 60 mL methanol solution containing $Zn(NO_3)_3 \cdot 6 H_2O$ (6.0, 4.0, 3.0, 2.0 or 0 mmol) and $Co(NO_3)_3 \cdot 6 H_2O$ (0.0, 2.0, 3.0, 4.0 or 6.0 mmol). Then 3.0 mmol of dimethylimidazole was added and stirred well. After the reaction, ZIF samples of different proportions and types can be grown in situ again on the surface of C-F@CuCo₂S₄. They are named C-F@CCS@ZIF8, C-F@CCS@ZIF8/67–2/1, C-F@CCS@ZIF8/67–1/1, C-F@CCS@ZIF8/67–1/2 and C-F@CCS@ZIF67 according to the ratio and type of their in-situ growth active substances.

2.1.4. Physical mixing of C-F@CuCo₂S₄ + ZIF8/67–1/1 sample was prepared

The C-F@CuCo₂S₄ and ZIF8/67–1/1 powders obtained in the above steps were added to a beaker containing 20 mL methanol, ultrasonic dispersion for 10 min, and then dried to obtain physically mixed C-F@CuCo₂S₄ + ZIF8/67–1/1 samples.

2.2. Evaluation of the photocatalytic activity

The degradation of CIP and reduction of Cr(VI) under visible light were used to evaluate the photocatalytic performance of the composites. Typically, 10 mg of composite photocatalyst is added to 50 mL of
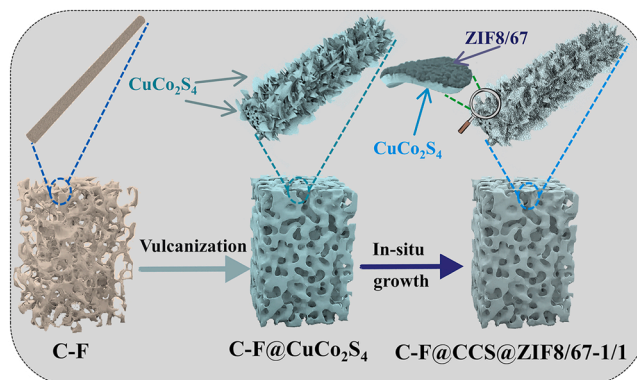
Scheme 1. Schematic diagram of the preparation of C-F@CCS@ZIF8/67–1/1 composites.

simulated contaminant solution containing CIP and Cr(VI) (both in 10 mg/L concentration). The simulated contamination solution was then transferred into a 50 mL cylindrical quartz tube and placed in a chamber equipped with a 500 W Xe lamp ($\lambda > 420$ nm, 4.81 W/cm^2) and a magnetic stirring (300 rpm) photochemical reactor. Before the photoreaction, it is necessary to stir the reaction solution under dark conditions for 30 min to make CIP and Cr(VI) fully enriched on the surface of the photocatalyst. During the experiment, 1 mL suspension was taken at intervals and the photocatalyst was removed by filtration. The concentration of CIP was measured by ultra-high liquid phase (HPLC) with 0.1% formic acid and acetonitrile as mobile phases at a ratio of 70:30 at a flow rate of 1 mL·min^{-1}, 10 μL samples were injected for each analysis, and the detection wavelength was 272 nm. The content of Cr(VI) was determined by a visible-ultraviolet spectrophotometer at 540 nm by diphenyl carbide colorimetry. The test of catalytic performance under UV light is consistent with that under visible light except for the light source (UV-lamp, 10 W, main wavelength at 254 nm, input light intensity of 2.0 W·m^{-2}). The effect of solution pH was

adjusted by adding 1 M NaOH and 1 M HCl. For studies involving natural organic matter, a contaminant solution containing 0–40 mg/L of humic acid (HA) was used for testing. In order to study the influence of inorganic ions on CIP degradation and Cr(VI) reduction, pollutant solutions containing 0–40 mM NaNO$_3$, Na$_2$SO$_4$, Na$_2$CO$_3$ and K$_2$HPO$_4$ were used for testing. A high-performance liquid chromatography-mass spectrometer (HPLC-MS) (Agilent 6530) was used to detect the photodegradation intermediates. The mobile phase was acetonitrile/water (80/20, v/v), the flow rate was 0.4 mL/min, and the sample size was 10 μL. Because there can be differences between test samples, all tests were carried out in three parallel sets of experiments and the average data from three samples and error bars were introduced for analysis.

3. Results and discussion

3.1. Microstructure and phase of the catalyst

Fig. 1a-b shows the initial surface morphology of C-F, showing the
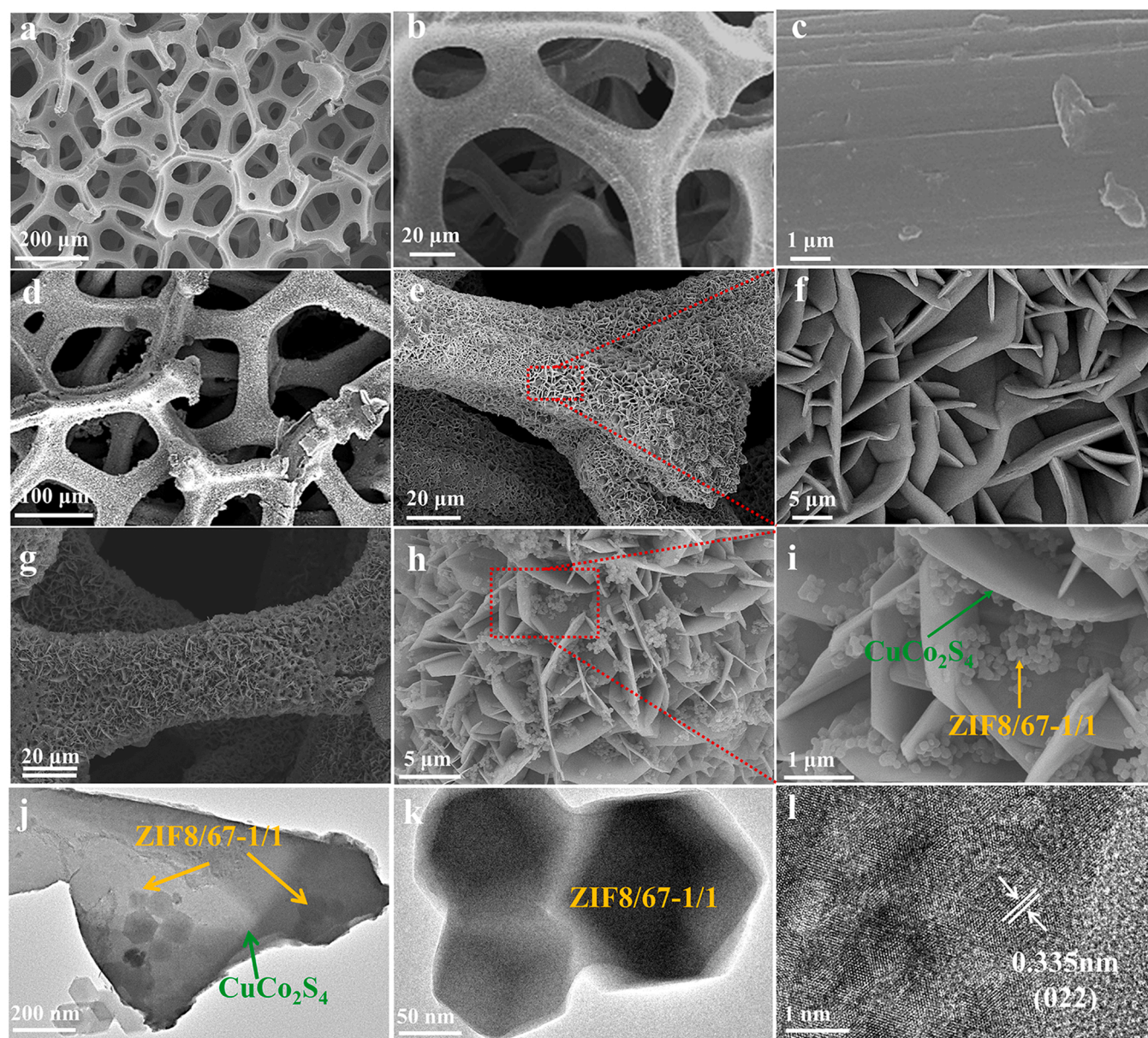

Fig. 1. (a-c) SEM image of the original C-F; C-F@CuCo$_2$S$_4$ SEM image at (d) low and (e-f) high magnification; (g, i) SEM image of C-F@CCS@ZIF8/67–1/1; (j) TEM images of C-F@CCS@ZIF8/67–1/1 heterogeneous structures; (k) TEM image of ZIF8/67–1/1; (l) lattice fringe spacing at C-F@CCS@ZIF8/67–1/1.

three-dimensional porous structure. Additional magnification reveals a smooth, impurity free surface (Fig. 1c), which provides a larger surface area and a more active location for the growth of active substances. As shown in Fig. S1a, the surface of C-F@ZIF8/67–1/1 becomes rough and there are obviously substances growing on the surface. Further observation by high-power SEM shows that the dodecahedron structure of ZIF8/67–1/1 is uniformly loaded on the surface of C-F (Fig. S1b). The vulcanized C-F@CuCo$_2$S$_4$ retained the original structure, but the surface became rough and CuCo$_2$S$_4$ vertical nanosheets were grown in-situ on the surface (Fig. 1d-e). As shown in Fig. 1f, CuCo$_2$S$_4$ nanosheets are distributed almost vertically and evenly on the smooth surface of C-F and are interconnected to form a connected network structure. This special network structure facilitates electron transport [22]. As shown in Fig. 1g-h, after the second step of in-situ growth, numerous ZIF8/67–1/1 nanoparticles were loaded on the surface of CuCo$_2$S$_4$ nanosheets. Furthermore, these nanoparticles are uniformly non-agglomerated and anchored to the surface (Fig. 1i). To further demonstrate the successful preparation of C-F@CCS@ZIF8/67–1/1, TEM and HRTEM were performed to confirm the structure of the heterostructures. TEM image (Fig. 1j) clearly shows that ZIF8/67–1/1 nanoparticles grow uniformly on the surface of CuCo$_2$S$_4$ nanosheets. This unique structure binds ZIF8/67–1/1 and CuCo$_2$S$_4$ together to form a heterojunction, which can accelerate the separation of photogenic carriers, enhance visible light absorption, and provide a wealth of active sites for photocatalytic reactions [23]. To further identify the element distribution of ZIF8/67–1/1 and CuCo$_2$S$_4$, local magnification of TEM images was performed, and Energy dispersive X-ray spectrometer (EDS) element mapping scanning was used, as shown in Fig. S2. It can be seen that Co elements exist on both ZIF8/67–1/1 and CuCo$_2$S$_4$, while Zn, N and C elements are only distributed on ZIF8/67–1/1, and Cu and S elements are only distributed on CuCo$_2$S$_4$, indicating that ZIF8/67–1/1 is successfully in-situ grown on the surface of CuCo$_2$S$_4$. Fig. 1k shows the TEM image of ZIF8/67–1/1 at high magnification, indicating that ZIF8/67–1/1 has a dodecahedral structure, which is consistent with the previous SEM image. From HRTEM images of the selected region, it can be seen that there is a clear set of parallel fringes with a lattice distance of 0.335 nm corresponding to the (022) crystal face of CuCo$_2$S$_4$ (Fig. 1l). In addition, the cross-section of the C-F@CCS@ZIF8/67–1/1 sample was treated by the ion thinning method. In the cross-section, FE-SEM tests showed that the active component was in close contact with C-F, indicating that the active substance was directly in-situ grown on the surface of C-F (Fig. 2a). Fig. 2b-h shows the EDS mapping maps of SEM images. The results show that Co and Cu elements are distributed over the whole

selected area, while Zn, S and N elements are distributed only on the surface of C-F. Since the test was performed on conductive carbon cloth, the C elements are distributed over the whole area. The above results indicate that ZIF8/67–1/1 and CuCo$_2$S$_4$ are directly grown on the surface of C-F. This result is consistent with the EDS distribution of TEM images. Therefore, there is no need to add a polymer binder (such as Naphthol, which increases contact and transfer resistance) to the system to prevent the nanosheet from falling off [24]. The appearance of the initial C-F, C-F@CuCo$_2$S$_4$ and C-F@CCS@ZIF8/67–1/1 composites are shown in Fig. S3. This structure is different from traditional powder materials and can be easily recycled after use without secondary pollution.

XRD analysis is used to evaluate the phase, crystal type and crystallinity of the composites. As shown in Fig. S4, C-F@ZIF-8 shows that the peaks at 7.5°, 10.4°, 12.7° and 18.4° correspond to (011), (002), (112) and (222) diffraction crystal planes respectively [25]. The peaks at 43.1° and 44.2° correspond to the diffraction peaks of Cu and Co in the cubic phase, respectively. C-F@ZIF8, C-F@ZIF8/67–2/1, C-F@ZIF8/67–1/1, C-F@ZIF8/67–1/2 and C-F@ZIF67 have the same diffraction peak, indicating that the cell parameters of the five samples are similar [26]. The XRD patterns of C-F, C-F@CuCo$_2$S$_4$ and C-F@CCS@ZIF8/67–1/1 are shown in Fig. 3a. Pure C-F has two peaks corresponding to elemental Cu and Co at 2θ values of 43.3° and 44.2°, respectively. The diffraction peaks of C-F@CuCo$_2$S$_4$ not only contain cubic phase cobalt and copper but also exist at 26.6°, 31.1° and 38.0°, corresponding to (002), (113) and (004) crystal planes of CuCo$_2$S$_4$ in cubic phase, respectively, indicating that CuCo$_2$S$_4$ successfully in-situ grow on C-F surface [27]. After in-situ growth of ZIF8/67 on the basis of C-F@CuCo$_2$S$_4$, C-F@CCS@ZIF8/67–1/1 not only exhibited the typical peaks of ZIF8/67 and CuCo$_2$S$_4$ but also retained the characteristic peaks of C-F, indicating that the composites were successfully synthesized in-situ again.

Fourier transform infrared (FT-IR) analysis provides functional group and structural information of C-F@ZIF8/67–1/1, C-F@CuCo$_2$S$_4$ and C-F@CCS@ZIF8/67–1/1. As shown in Fig. 3b, the typical peaks of C-F@ZIF8/67–1/1 at 424 and 417 cm^{-1} are caused by stretching vibrations of Co-N and Zn-N, respectively, while peaks at 1590 cm^{-1} and 1420 cm^{-1} correspond to stretching vibrations of C=C and C=N [28]. The peaks of C-F@CuCo$_2$S$_4$ near the 500–1200 cm^{-1} region correspond to the stretching and bending vibrations of the Cu-S and Co-S bonds [29]. For C-F@CCS@ZIF8/67–1/1 samples, the main characteristic peaks of ZIF8/67 and CuCo$_2$S$_4$ show a slight peak shift towards a low wave number. These changes confirm a tight interface contact between
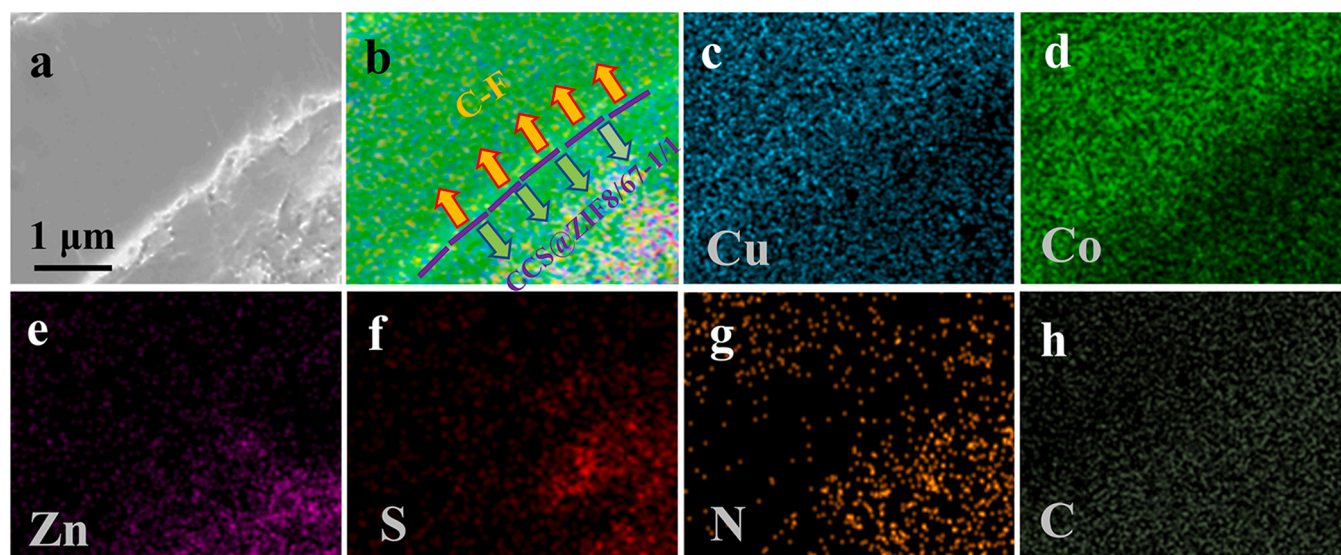

Fig. 2. SEM images of (a) cross-section of C-F@CCS@ZIF8/67–1/1 and (b-h) corresponding EDS mapping images.
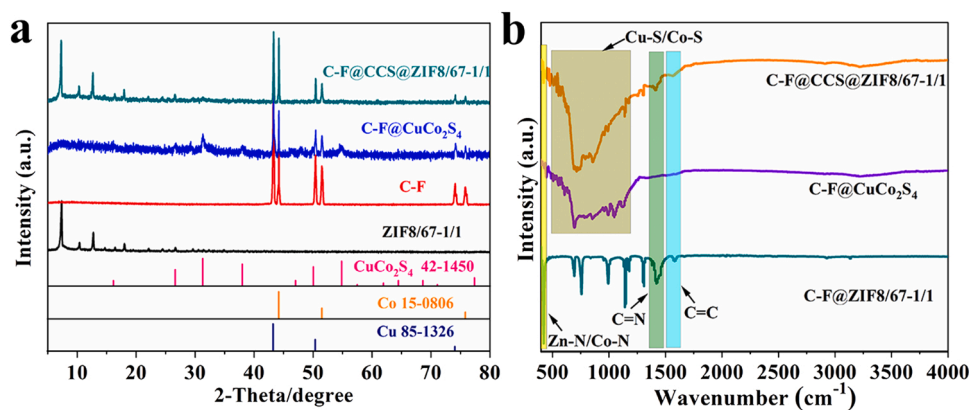
Fig. 3. (a) XRD patterns and (b) FT-IR spectrum of the prepared samples.

ZIF8/67 and CuCo$_2$S$_4$.

The specific surface areas and porous structures of C-F@CuCo$_2$S$_4$ and C-F@CCS@ZIF8/67–1/1 catalysts were analyzed by N$_2$ adsorption-desorption curves. C-F@CuCo$_2$S$_4$ showed a typical IV isotherm, while C-F@CCS@ZIF8/67–1/1 showed a hybrid isotherm of type I/IV (Fig. 4a). According to the formula, C-F@CCS@ZIF8/67–1/1's

Brunauer-Emmett-Teller (BET) surface area is about 624.4 m^2·g^{-1}. At the same time, the pore size distribution (PSD) of C-F@CCS@ZIF8/67–1/1 sample was estimated by using nonlinear density functional theory (NL-DFT). As shown in Fig. 4b, the prepared C-F@CCS@ZIF8/67–1/1 catalyst has pore size distribution in the range of 1–10 nm and has both microporous and mesoporous structures [30]. This unique
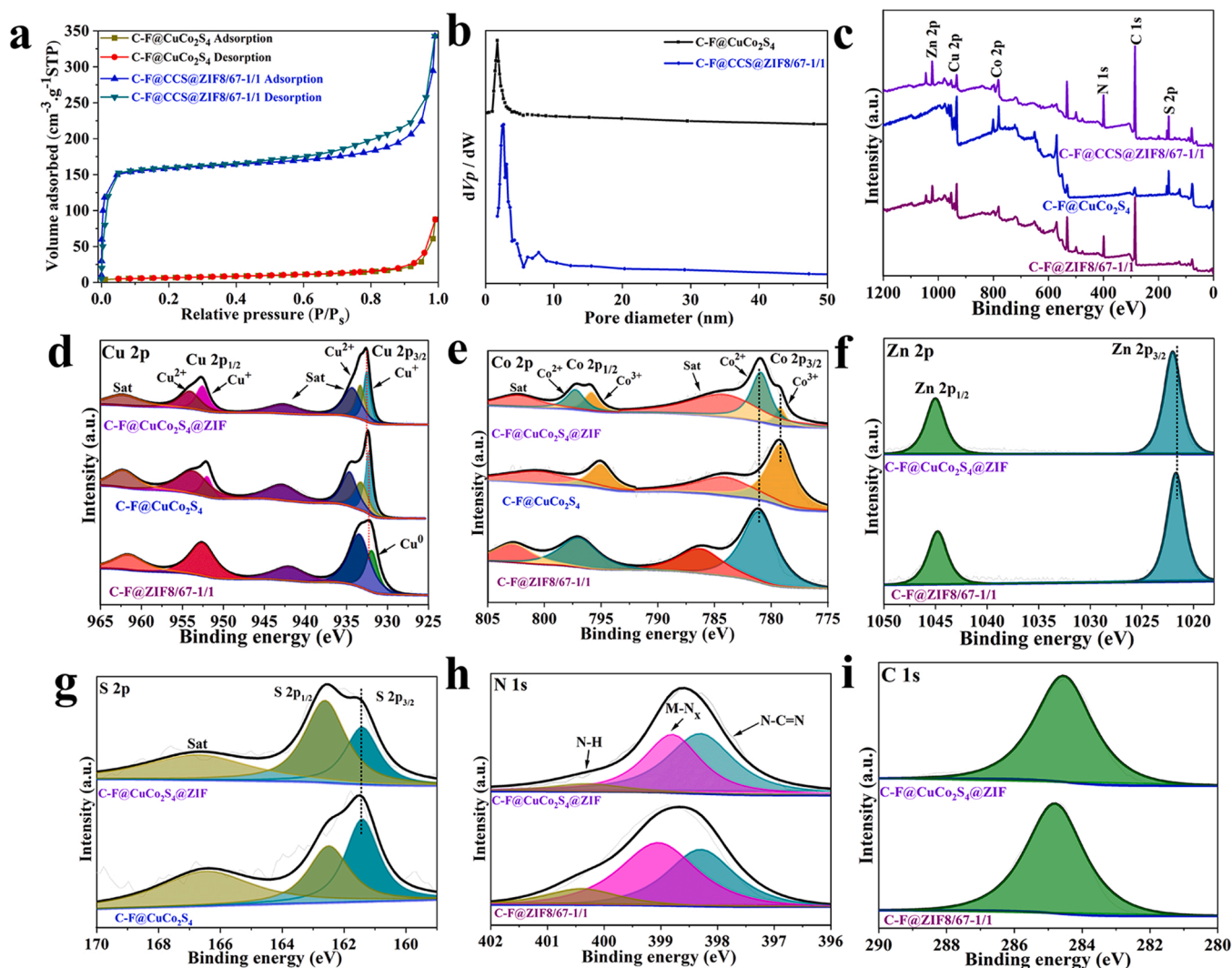

Fig. 4. (a, b) N$_2$ adsorption-desorption isothermal pore size dispersion; (c) X-ray photoelectron spectroscopy (XPS) survey spectra; High-resolution spectra of (d) Cu 2p, (e) Co 2p, (f) Zn 2p, (g) S 2p, (h) N 1 s and (i) C 1 s.

structure with both mesoporous and microporous structures is known to ensure the successful enrichment of pollutants, as the former attracts adsorbent molecules and the latter accelerates the adsorption process by providing channels [31].

The chemical components and valence states of the composite catalyst surface were analyzed by XPS. The measured XPS survey spectrum of C-F@ZIF8/67–1/1, C-F@CuCo$_2$S$_4$ and C-F@CCS@ZIF8/67–1/1 are shown in Fig. 4c, where C-F@CCS@ZIF8/67–1/1 contains Co and the presence of Cu, Zn, S, C and N, while C-F@ZIF8/67–1/1 and C-F@CuCo$_2$S$_4$ do not contain S and Zn, respectively. The high-resolution spectrum of Cu 2p in C-F@ZIF8/67–1/1 shows that the binding energy at 932.2 and 952.1 eV corresponds to Cu 2p$_{3/2}$ and Cu 2p$_{1/2}$, and the peak at 931.8 eV after peak fitting indicates that Cu 2p exists in the form of Cu^0, and the valence state of Cu does not change after recombination [32]. For the Cu 2p peaks of C-F@CuCo$_2$S$_4$ and C-F@CCS@ZIF8/67–1/1 samples (Fig. 4d), there are two peaks at 932.9 eV and 952.8 eV, and the binding energy is 19.9 eV, corresponding to Cu 2p$_{3/2}$ and Cu 2p$_{1/2}$. The peaks of the Cu 2p spectrum at 932.2 and 952.2 eV can be attributed to Cu$^+$, while the peaks at 933.3 and 953.9 eV can be attributed to Cu^{2+} [33]. Moreover, the Cu 2p peak of C-F@CCS@ZIF8/67–1/1 moves towards high energy, which may be due to the formation of heterojunction, resulting in lattice strain at the interface between ZIF8/67–1/1 and CuCo$_2$S$_4$ [34]. The Co 2p spectrum of C-F@CCS@ZIF8/67–1/1 (Fig. 4e) has two main peaks at 780.9 and 796.8 eV, corresponding to Co 2p$_{3/2}$ and Co 2p$_{1/2}$, respectively. The spin separation between Co2p$_{3/2}$ and Co 2p$_{1/2}$ is about 15.9 eV, indicating the presence of Co^{2+} and Co^{3+}. The deconvolution peaks at 780.9 and 797.4 eV correspond to the Co^{3+} state. Similarly, the deconvolution peaks at 779.0 and 796.2 eV correspond to the Co^{2+} state [35]. In the Zn 2p spectrum, two major peaks at 1021.8 and 1044.6 eV are attributed to Zn^{2+}, and C-F@CCS@ZIF8/67–1/1 also moves towards higher energies (Fig. 4f) [36]. The S 2p spectrum in Fig. 4g has two major peaks at 161.4 eV and 162.6 eV, which are S 2p$_{3/2}$ and S 2p$_{1/2}$, respectively, proving the existence of S^{2-} [37]. Similar to Cu 2p also moves to higher energies

because of heterojunction formation. In addition, the N 1 s high-resolution XPS spectra of C-F@ZIF8/67–1/1 and C-F@CCS@ZIF8/67–1/1 (Fig. 4h) show three chemical states of N-metallic bond, pyridine N and N oxide, with binding energies of 399.1 eV, 398.3 eV and 400.4 eV, respectively, which are similar to ZIF8/67 reported in the literature [38]. Fig. 4i shows the deconvolution of XPS spectra with peaks for C 1 s. The peak value centered at 284.6 eV corresponds to the C-C/C=C peak of ZIF8/67 [39].

3.2. Simultaneous removal of CIP and Cr(VI) by photocatalysis

The photocatalytic properties of the composite samples were tested by simultaneous CIP degradation and Cr(VI) reduction. Before irradiation, the adsorption experiment was carried out in the dark, and the results were shown in Fig. 5a. The concentrations of CIP and Cr(VI) barely changed after 30 min, indicating that the solution reached the adsorption-desorption equilibrium after 30 min treatment in the dark. As shown in Fig. 5b, after 90 min irradiation under visible light, the photocatalytic performance of the monomer is lower than that of the composite photocatalyst. At the same time, the removal rates of CIP and Cr(VI) solution by C-F@CuCo$_2$S$_4$ monomer material were only 69.7% and 43.8%, respectively. Similarly, the removal rates of C-F@ZIF8/67–1/1 were only 78.1% and 75.6%, respectively. Importantly, C-F@CCS@ZIF8/67–1/1 has the highest catalytic efficiency, which can achieve 97.2% CIP degradation and 96.5% Cr(VI) reduction after 90 min illumination, while the photocatalytic performance of C-F@CCS@ZIF8, C-F@CCS@ZIF8/67–2/1, C-F@CCS@ZIF8/67–1/2 and C-F@CCS@ZIF67 is reduced. The reason may be that the ratio of ZIF8/67–1/1 has the highest concentration of oxygen vacancy. At the same time, this ratio has the best charge transfer ability and reduces the inhibition of photogenic charge recombination. In addition, the composite catalyst prepared under this ratio has uniform dispersion and high specific surface area, which can accelerate the enrichment of pollutants and provide enough reactive sites. Pseudo-first-order models was used to
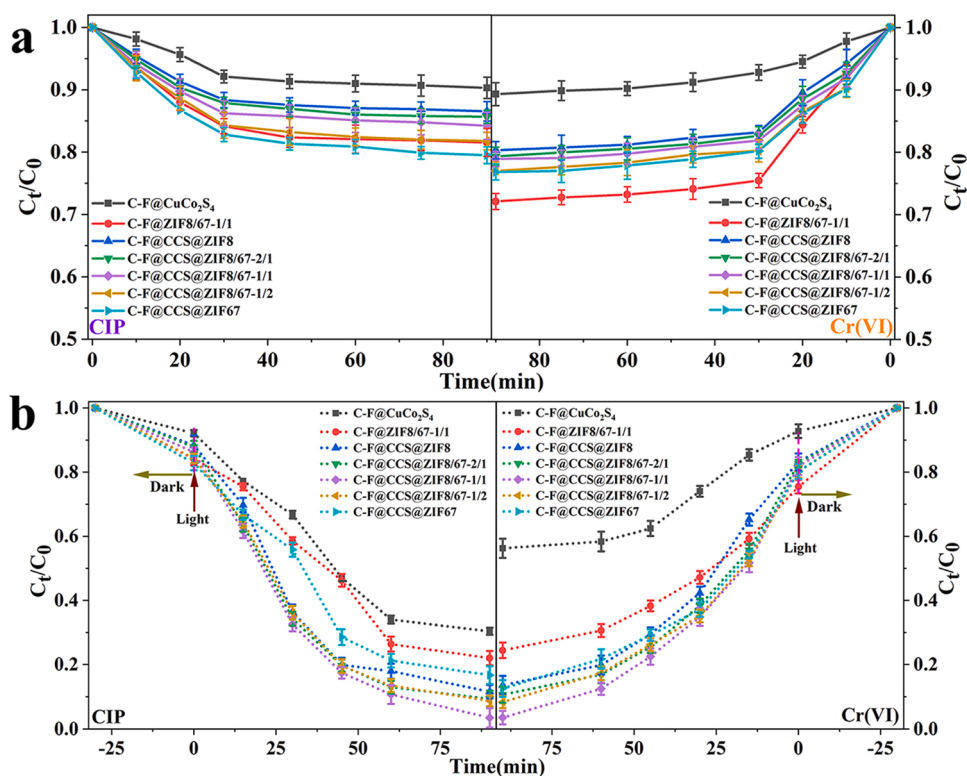

Fig. 5. The adsorption efficiency of different catalysts in (a) dark environment and (b) catalytic efficiency in dark + light environment under CIP and Cr(VI) coexistence.

simulate the kinetics of photocatalytic removal of pollutants, expressed as $kt = -\ln(C_0/C_t)$ [40]. Slope (k) indicates the photocatalytic performance of the photocatalyst. As shown in Fig. S5 and Table S1, it is obvious that the kinetic constants of CIP and Cr(VI) are consistent with the results of the removal rate. In order to confirm the catalytic activity of catalysts under UV light, the synchronous removal properties of CIP and Cr(VI) were evaluated by using a visible cutoff filter. As shown in Fig. S6, the performance of all catalysts decreased under UV irradiation, C-F@CCS@ZIF8/67–1/1 showed the highest catalytic performance, CIP removal rate was 98.2% and Cr(VI) reduction rate was 99.8% after 30 min dark adsorption and 150 min light exposure. Under UV conditions, C-F@CCS@ZIF8 showed the worst photocatalytic performance, with CIP and Cr(VI) removal rates of 48.9% and 41.9%, respectively. The above results showed that the addition of Co ions improved the catalytic performance of the synthesized catalyst under UV light. At the same time, we tested the synchronous removal performance of CIP and Cr(VI) of the composite material synthesized by physical mixture of C-F@CuCo2S4 and ZIF8/67–1/1. The degradation rate of CIP and reduction rate of Cr(VI) of the composite material were only 58.7% and 51.8% respectively (Fig. S7). As shown in Fig. S8, many ZIF8/67–1/1 particles appeared in the residual solution after the physical mixing reaction, while there was no suspended matter in the residual solution of C-F@CCS@ZIF8/67–1/1 sample. Therefore, the reason for the poor performance may be that the insufficient binding force between the two active components of the physical mixing led to the loss of active substances, which reduced the catalytic activity of the material. In conclusion, the constructed C-F@CCS@ZIF8/67–1/1 composite photocatalyst has excellent photocatalytic performance. The photocatalytic properties of C-F@CCS@ZIF8/67–1/1 composites were studied by removing CIP or Cr(VI) in visible light. Controlled experiments exclude photolysis under natural conditions. As shown in Fig. S9, no significant removal of CIP and Cr(VI) was observed in the absence of a photocatalyst, indicating that no self-degradation of CIP and Cr(VI) occurred in the absence of a photocatalyst. After 30 min of dark adsorption and 90 min of visible light exposure, the degradation rate of CIP single pollutant removal by C-F@CCS@ZIF8/67–1/1 was 36.6%. At the same time, we compared the performance of reducing Cr(VI) single pollutant in C-F@CCS@ZIF8/67–1/1, and the reduction rate of CIP was 39.7% after 90 min of visible light irradiation after dark adsorption. The photocatalytic degradation rate of CIP reached 97.2% and the reduction rate of Cr(VI) was 96.5% in the presence of both pollutants. The enhancement of C-F@CCS@ZIF8/67–1/1 photocatalytic performance in pollutant coexistence systems can be attributed to the synergistic effect between photocatalytic reduction and oxidation processes. In co-existing systems, CIP acts as a photogenerated hole scavenger and is oxidized, while Cr(VI) acts as a photogenerated electron acceptor and is reduced, and the interaction reduces the photoinduced e^-/h^+ recombination [41].

3.3. Photocatalytic mechanism

The light absorption capacity of different composites was tested by the ultraviolet-visible absorption method. As shown in Fig. 6a, CF@ZIF sample doped with Co ion not only has strong ultraviolet absorption capacity at 220–350 nm, but also shows strong visible light absorption capacity between 450 and 650 nm, while C-F@ZIF-8's absorption band is mainly below 250 nm, showing a strong UV absorption capacity. This is consistent with previously reported results. Interestingly, the bimetallic mixed samples showed similar absorption peaks to C-F@ZIF67 [42]. It can be observed from the absorption spectrum that the absorption edge of pure C-F@CuCo2S4 is around 565 nm [43]. The absorption intensity of the composite sample in the visible range is significantly enhanced when compared to that of pure C-F@ZIF, as illustrated in Fig. S10a. This indicates that the in-situ growth of ZIF on the photocatalyst enhances its visible light absorption. Furthermore, the absorption capacity of the sample doped with Co^{2+} ion is better than that of the sample with only Zn^{2+} ion. Samples doped with Zn^{2+}/Co^{2+} ions have a broader absorption range in the visible region compared to those doped with pure Co^{2+} ions. The absorption band of the sample C-F@CCS@ZIF8/67–1/1 is found to be the largest in the edge range of ultraviolet and visible light when the Zn^{2+}/Co^{2+} ion ratio is 1/1. The ultraviolet and visible light absorption capacity of C-F@CCS@ZIF8/67–1/1 composite photocatalyst is enhanced, leading to improved photocatalytic performance [44]. C-F@CCS@ZIF shows different apparent colors, C-F@CCS@ZIF8 is grayish white, while materials added with Co^{2+} ion are all purplish black, and its color gradually changes from light purple to bright purple with the increase of Co^{2+} ion (Figs. S11). The Tauc graph is obtained according to the Kubelka-Munk formula of Eq. (1) [45]:

$$\alpha h\nu = A\left(h\nu - E_g\right)^{n/2} \tag{1}$$

In the symbols of the formula, α represents the absorption coefficient, h represents Planck's constant, v represents the optical frequency, A is the proportionality constant related to the material, and E_g represents the bandgap energy. In addition, n indicates the nature of the semiconductor transition process (C-F@CuCo2S4 is a direct semiconductor: n = 1; C-F@ZIF is an indirect semiconductor: n = 4). As shown in Fig. 6 b and c, E_g values of C-F@ZIF8, C-F@ZIF8/67–2/1, C-F@ZIF8/67–1/1, C-F@ZIF8/67–1/2, C-F@ZIF67 and C-F@CuCo2S4 are estimated to be 5.09 3.38, 3.30, 3.37, 3.52 and 2.23 eV respectively. When ZIF is grown in-situ to form heterojunction materials at C-F@CuCo2S4, the band gap decreased significantly. Moreover, when the ratio of Zn^{2+}/Co^{2+} ions is 1/1, it has the narrowest band gap, and the enhanced visible light absorption helps to improve the photocatalytic efficiency (Fig. S10b) [46].

The flat band potential (Ef) of several composites was evaluated by the Mott-Schottky diagram, as shown in Fig. S12. The Ef value is obtained by extending the tangent line along the linear part of the Mott-Schottky curve at different frequencies and different materials to the
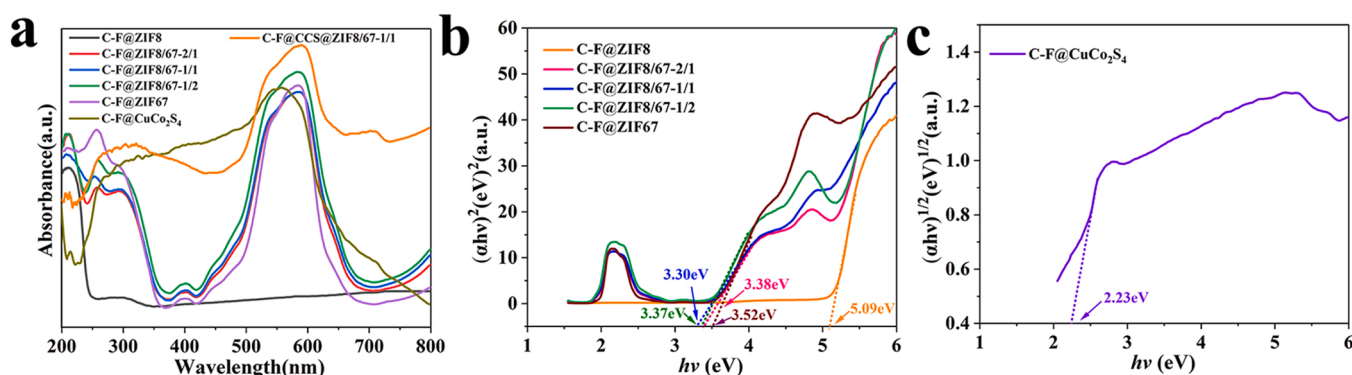

Fig. 6. (a) Ultraviolet-visible diffuse reflection spectra of the prepared photocatalyst and (b, c) corresponding Tauc diagrams.

intersection of the abscissa. According to previous literature, the conduction band edge potential (E_{CB}) of an n-type semiconductor is less than about 0.1 eV compared with Ef, and the slope of C-F@ZIF is positive, so it is an n-type semiconductor. The E_{CB} (lowest unoccupied molecular orbital (LUMO)) of C-F@ZIF8, C-F@ZIF8/67–2/1, C-F@ZIF8/67–1/1, C-F@ZIF8/67–1/2, C-F@ZIF67 were calculated by its flat band formula to be − 0.50, − 0.54, − 0.70, − 0.92 and − 1.01 eV (vs. NHE), respectively. The valence band potential (E_{VB}) of a p-type semiconductor is about 0.1 eV larger than Ef. The negative slope of C-F@CuCo$_2$S$_4$ is typical of a p-type semiconductor, and E_{VB} is 1.15 eV (vs. NHE) calculated according to the formula [47]. According to the formula Eq. (2), E_{VB} and E_{CB} of different materials can be obtained [48]:

$$E_{CB} + E_g = E_{VB} \qquad (2)$$

According to the formula, the E_{VB} (highest occupied molecular orbital (HOMO)) of C-F@ZIF8, C-F@ZIF8/67–2/1, C-F@ZIF8/67–1/1, C-F@ZIF8/67–1/2, C-F@ZIF67 were 4.59, 2.84, 2.60, 2.45 and 2.51 eV (relative to NHE), respectively, while the E_{CB} of C-F@CuCo$_2$S$_4$ was − 1.08 eV (relative to NHE). As shown in Fig. S13, for the C-F@CCS@ZIF8/67–1/1 complex catalyst, there are two linear regions in the Mott-Schottky diagram, shown as an inverted "V" shape. This is due to the p-n heterojunction formed after the coupling of n-type ZIF8/67–1/1 and p-type CuCo$_2$S$_4$, which leads to the Fermi level displacement, that is, the displacement of the flat band potential [49].

In order to study the photoexcited charge separation and transfer process at CuCo$_2$S$_4$/ZIF8/67–1/1 interface, SPV technology is used to study the photoelectric performance of the original C-F@CuCo$_2$S$_4$ and C-F@ZIF8/67–1/1, as shown in Fig. 7a. The SPV response is caused by a transition between the energy bands of the material. A simple diagram of the SPV test method is shown in the illustration. The top electrode is the blank FTO, which is connected to the amplifier, and the positive response means that the hole is transferred to the top electrode. For C-F@ZIF8/67–1/1 sample, the response range of SPV is about 220–350 nm and 450–650 nm, which is consistent with the original UV-Vis absorption spectrum response range. The positive response of the

SPV indicates an n-type semiconductor [50]. For C-F@CuCo$_2$S$_4$, the response range is about 250–565 nm wavelength, corresponding to the spectral response range of C-F@ZIF8/67–1/1. And the negative response of SPV means a p-type semiconductor [51].

The separation and recombination of photogenerated electron-hole pairs in the sample is an essential factor determining the performance of the photocatalyst, so the carrier separation efficiency of different materials was tested. PL spectrum (Fig. 7b) shows the recombination of electron-hole pairs. The formation of heterojunction between ZIF8/67–1/1 and CuCo$_2$S$_4$ can effectively promote the spatial separation of photogenerated carrier pairs and significantly reduce the PL strength of composites [52]. In addition, TR-PL spectra is used to evaluate the recombination rate of photogenerated carriers, and the fitted emission attenuation curve and the calculated average PL lifetime (τ_{avg}) are shown in Fig. 7c. τ_{avg} is calculated by the formula: $\tau_{avg} = \tau_1 \times A_1 + \tau_2 \times A_2$. According to the calculation results, the τ_{avg} of C-F@CCS@ZIF8/67–1/1 was 3.09 ns, which has the highest fluorescence lifetime. The prolongation of fluorescence lifetime indicates that the photogenerated electron-hole pair can be effectively separated, which can provide more active components (free radicals, holes, electrons) for the redox reactions, which promotes the photocatalytic reaction efficiency [53].

Fig. 7d shows the photocurrent response of a series of photocatalytic composites. The generation and disappearance of photocurrent are rapidly switched on and off with the light. In addition, the peak value of the transient photocurrent response remains stable after the light is turned on, which means that the photocatalyst material can provide sufficient electron-hole pairs. The photocurrent value of C-F@CCS@ZIF8/67–1/1 is greatly higher than that of other photocatalytic systems, which may be due to the formation of heterojunction and the existence of oxygen vacancy affecting the electron transport mechanism [54].

The AC impedance of different materials was studied by electrochemical impedance spectroscopy (EIS). In EIS, the semicircle at high frequency corresponds to the charge transfer resistance (Rct), and the
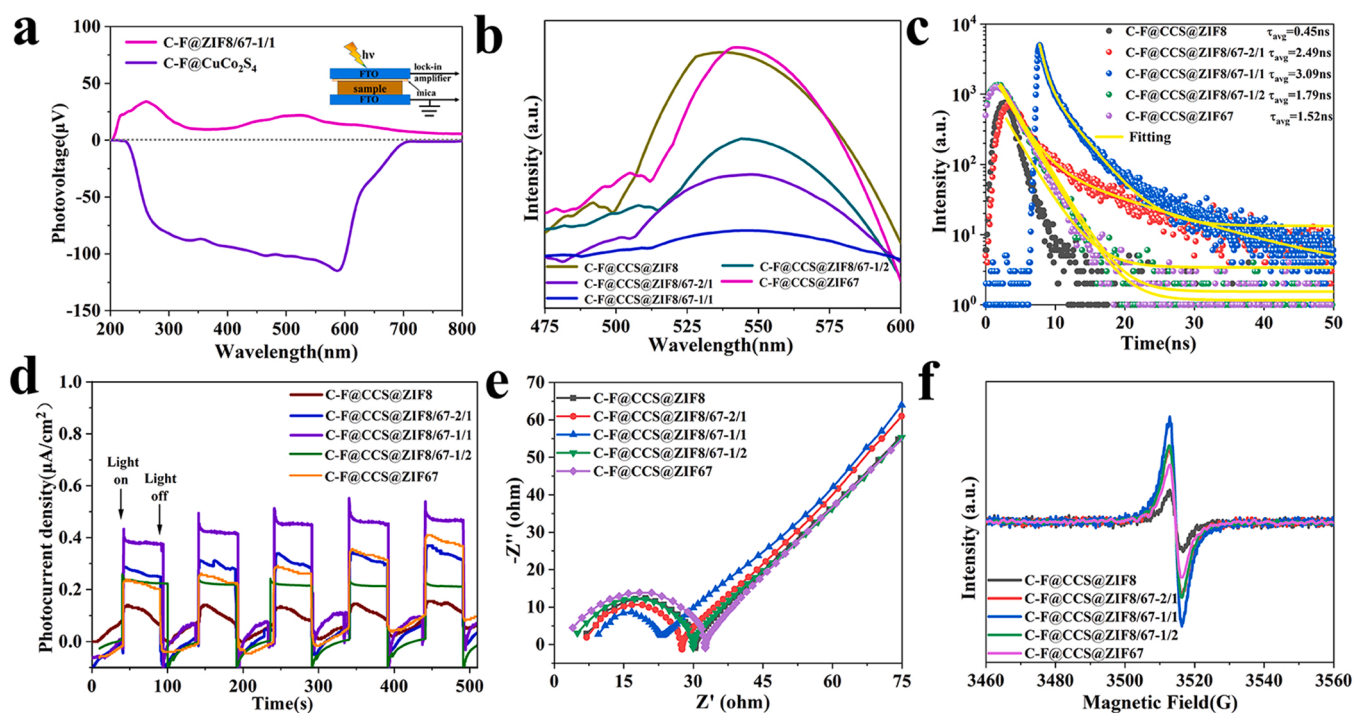

Fig. 7. (a) SPV spectra of C-F@CuCo$_2$S$_4$ and C-F@ZIF8/67–1/1 samples; A series of photochemical characterization of C-F@CCS@ZIF8, C-F@CCS@ZIF8/67–2/1, C-F@CCS@ZIF8/67–1/1, C-F@CCS@ZIF8/67–1/2 and C-F@CCS@ZIF67 by (b) PL spectrum, (c) TR-PL decay spectrum, (d) transient photocurrent response, (e) EIS, (f) EPR.

size of the radius of the arc indicates the charge transfer efficiency at the semiconductor-electrolyte interface. As shown in Fig. 7e, C-F@CCS@ZIF8/67–1/1 has the smallest circular radius, indicating that C-F@CCS@ZIF8/67–1/1 exhibits a low charge transfer resistance in photocatalytic reactions [55]. In addition, the Rct of all the electrodes is considerably smaller than those of traditional powder photocatalytic materials, which may be due to the fact that cobalt-copper foam, as a base material with excellent electrical conductivity, allows rapid transport and separation of electrons to improve the photocatalytic activity [56]. To obtain information on potential defects in different composite samples, electron paramagnetic resonance (EPR) tests were performed. As shown in Fig. 7f, all samples exhibit a single characteristic signal at g = 2.003, which can usually be attributed to electrons captured by oxygen vacancies [57]. It is worth noting that the signal intensity of the samples with different Zn^{2+}/Co^{2+} ratios is different. The EPR signal intensity is the strongest when the Zn^{2+}/Co^{2+} ratio is 1/1, indicating the highest oxygen vacancy concentration under this ratio condition [58]. Oxygen vacancies can provide more active sites and accelerate photocarrier transfer during photocatalysis [59].

In order to determine the active components of C-F@CCS@ZIF8/67–1/1 composite photocatalyst in the coexistence of CIP and Cr(VI), ESR and free radical capture experiments were conducted [60]. As shown in Fig. 8a, with the addition of ethylenediaminetetraacetic acid disodium salt (EDTA-2Na) and 1,4-Benzoquinone (P-BQ), the removal efficiency of CIP decreases significantly, indicating that h^+ and $\bullet O^{2-}$ are the main active substances for CIP removal. The removal efficiency of CIP was slightly increased by adding potassium bromate (PB) to capture e^-, which also proved that h^+ was the main active species for the removal of CIP because electrons and holes appeared in pairs. The degradation efficiency of CIP did not change after the addition of

tert-butanol (TBA), indicating that the $\bullet OH$ was not an active species. As shown in Fig. 8b, in the Cr(VI) reduction process, the reduction efficiency is slightly improved when EDTA-2Na is added, while the reduction efficiency decreases with the addition of PB. This phenomenon indicates that e^- is the only active species in Cr(VI) reduction. In order to further confirm the above main active substances obtained in the photocatalytic process, ESR analysis was performed, and the results are shown in Fig. 8c-d. As expected, DMPO-$\bullet O^{2-}$ and TEMP-h^+ of C-F@CCS@ZIF8/67–1/1 samples showed distinct characteristic signals under visible light irradiation [61]. The photocatalytic degradation of CIP and reduction of Cr(VI) by $\bullet O^{2-}$, e^- and h^+ were determined to play a major role through free radical capture experiment and ESR characterization.

The potential mechanism of forming p-n heterojunction interface to enhance photocatalytic activity was further elucidated by density functional theory (DFT) calculation. The structural models at different observation locations are shown in Fig. S14, and the ratio of Zn/Co atoms in the center of ZIF8/67 is 1/1. As shown in Fig. 9a, the calculated band gap value of $CuCo_2S_4$ crystal is 1.90 eV, which is close to the experimental value. ZIF8/67–1/1 is an indirect band-gap structure. The valence band top (VBM) and conduction band edge (CBM) are located at the Γ and N points in the Brillouin region, respectively, with a band gap value of 1.43 eV (Fig. 9b). The band map of the calculated composite structure shows that the band gap value is further reduced relative to $CuCo_2S_4$ and ZIF8/67–1/1. This indicates that after recombination, the energy levels near the Fermi level gradually distributed continuously and even the band gap disappeared, which is conducive to the conduction of electrons and the increase of activity (Fig. 9c) [62]. The calculation of the state density (TDOS) of $CuCo_2S_4$ crystal is shown in Fig. 9d. VBM mainly contributes to the 3d orbit of Co. CBM is mainly
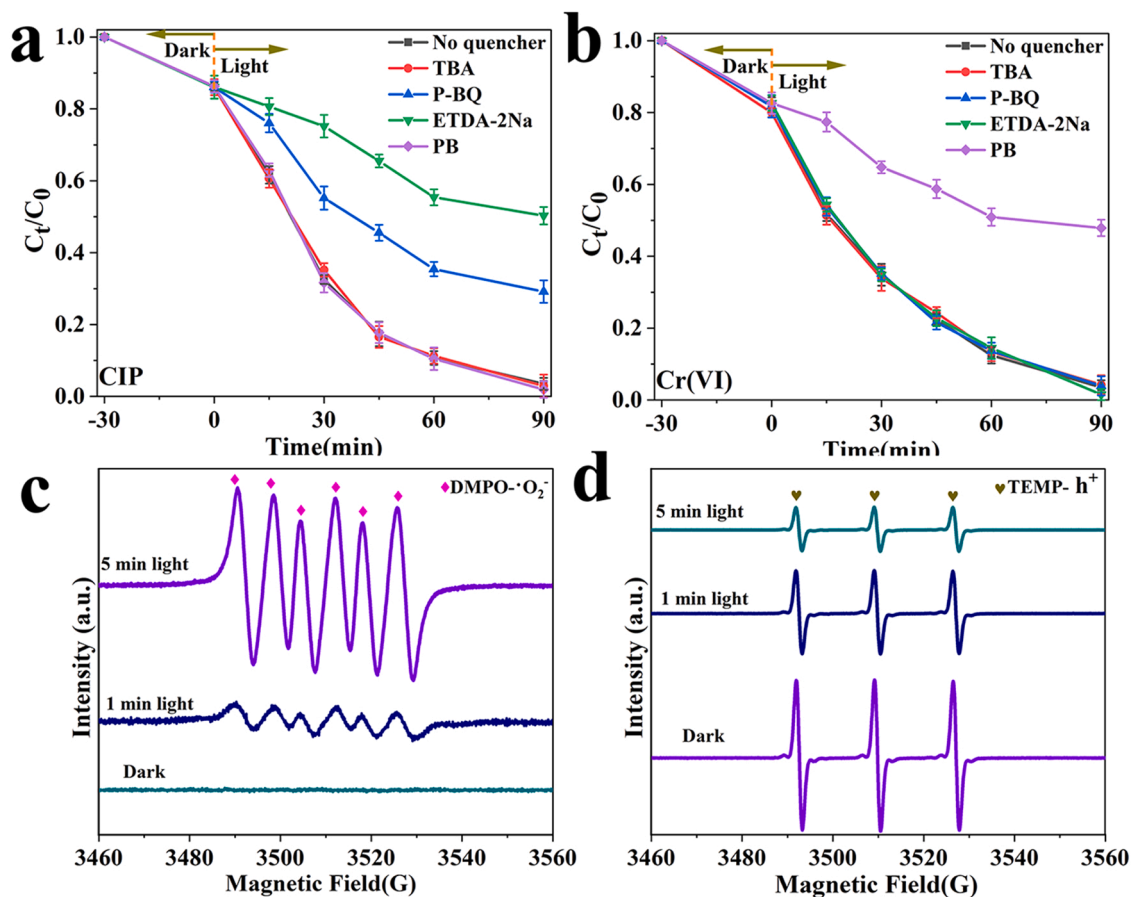

Fig. 8. (a) The removal efficiency of CIP and (b) reduction efficiency of Cr(VI) in the presence of different scavengers; ESR spectra of (c) DMPO-$\bullet O^{2-}$ and (d) TEMP-h^+.
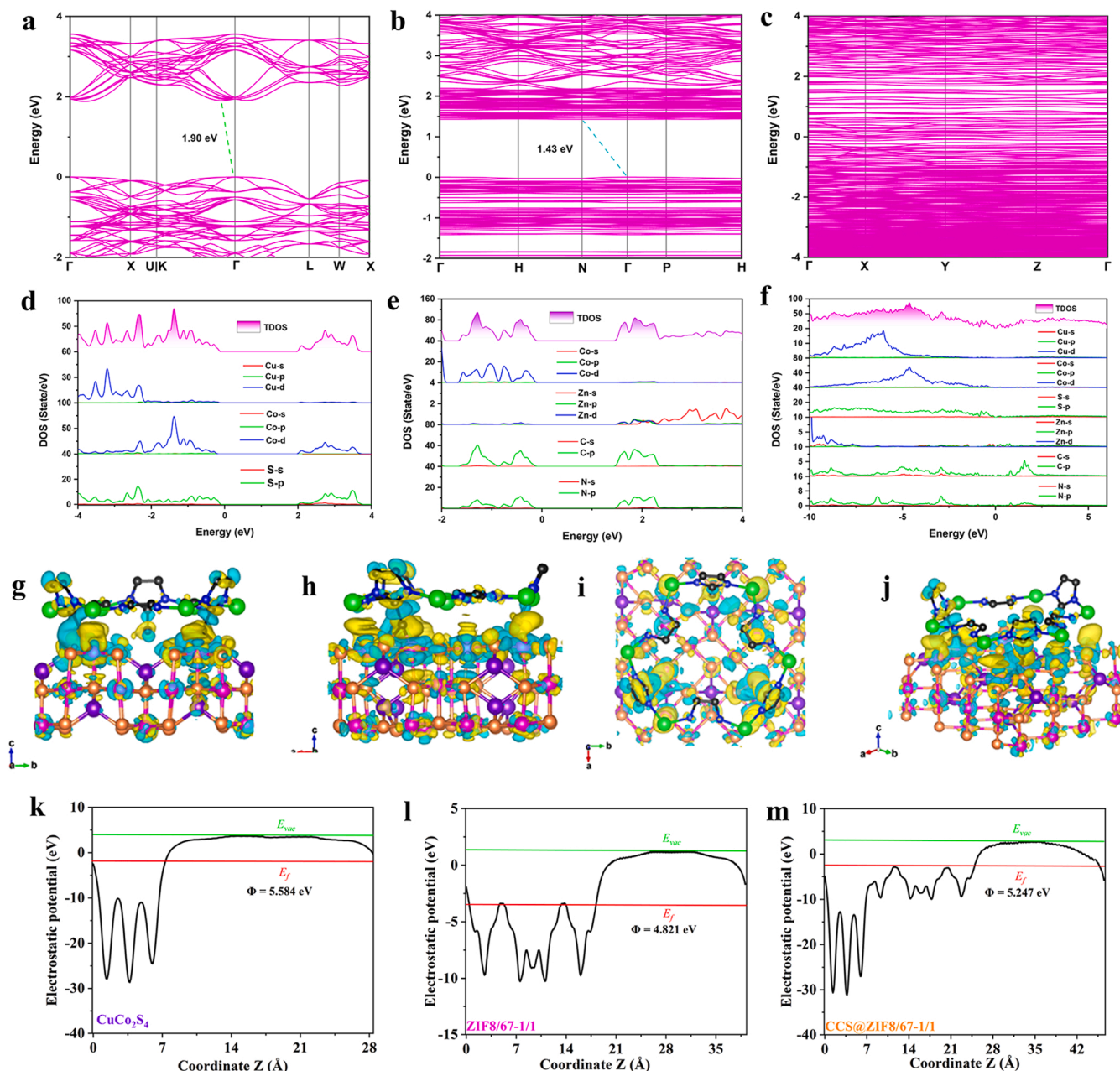
Fig. 9. The band structures of (a) CuCo$_2$S$_4$, (b) ZIF8/67–1/1 and (c) after contact were calculated; TDOS of (d) CuCo$_2$S$_4$, (e) ZIF8/67–1/1 and (f) after contact; (g-j) Spatial charge distribution of C-F@CCS@ZIF8/67–1/1; Work function of (k) CuCo$_2$S$_4$, (l) ZIF8/67–1/1 and (m) CCS@ZIF8/67–1/1.

contributed by the 3d orbital components of Co and the 3p orbital components of S. TDOS of ZIF8/67–1/1 is shown in Fig. 9e. VBM mainly contributes to 2p of C and 3d orbital components of Co, while CBM mainly contributes to 2p of C and 2p of N. TDOS after composite is shown in Fig. 9f. VBM mainly contributes to the orbital components of elements in CuCo$_2$S$_4$, while CBM mainly contributes to the orbital components of elements in ZIF8/67–1/1. This indicates the reallocation of electron orbitals in the composite structure. In addition, the band gap is reduced to almost disappearance which further increases the ability of electron transport. The electron orbital arrangement of VBM and CBM indicates that both CuCo$_2$S$_4$ and ZIF8/67–1/1 are involved in the charge transport process [63]. The spatial charge distribution is shown in Fig. 9g-j, where the yellow region represents the gained charge and the cyan region represents the lost charge. It can be seen that CuCo$_2$S$_4$ and ZIF8/67–1/1 have obvious charge exchange, which further confirms that charge transfer is achieved near the contact surface, thus improving

the catalytic activity. These results also indicate that electrons tend to transfer from ZIF8/67–1/1 to CuCo$_2$S$_4$, and an internal electric field can be formed at the contact interface until electron diffusion reaches a state of equilibrium [64]. The result of space charge distribution is consistent with that of TDOS. According to the DFT calculation results shown in Fig. 9k and l, the work functions of CuCo$_2$S$_4$ and ZIF8/67–1/1 are determined to be 5.584 eV and 4.821 eV, respectively. Thus, negative charges on ZIF8/67–1/1 tend to migrate to CuCo$_2$S$_4$ on contact [65]. Moreover, the simulated Ef values of CuCo$_2$S$_4$ and ZIF8/67–1/1 are − 1.828 eV and − 3.495 eV, respectively. Due to the difference in Ef levels, electrons tend to transfer from the ZIF8/67–1/1 surface to the surface in contact with CuCo$_2$S$_4$, which is consistent with the spatial charge distribution results [66]. In addition, the Ef of CuCo$_2$S$_4$ and ZIF8/67–1/1 rearranged equilibrium after contact, and their Ef was in between (Fig. 9m). After Fermi equilibrium is reached, a space charge region with strong internal electric field can be formed, which

effectively promotes the separation of photogenerated carriers in the photocatalytic reaction.

According to the DFT calculation, the contact interface between ZIF8/67–1/1 and $CuCo_2S_4$ may form an internal electric field, which promotes the separation of photogenerated carriers. Therefore, the characterization of internal electric field is of great significance to reveal its mechanism. C-F@$CuCo_2S_4$ and C-F@CCS@ZIF8/67–1/1 samples of the same thickness were selected to accurately compare their potential differences. As shown in Fig. 10a-c, the initial $CuCo_2S_4$ sample is a two-dimensional plane with almost no height difference. After in-situ growth of ZIF8/67–1/1 on the surface, many convex spots appeared on the surface corresponding to ZIF8/67–1/1 particles (Fig. 10d-f). The average surface voltage (SP) of $CuCo_2S_4$ characterized by KPFM is 230 mV, which is significantly lower than that of CCS@ZIF8/67–1/1 sample with an average surface voltage of 454 mV (Fig. 10g, h). The increase in SP is related to the internal electric field caused by the interface charge movement after contact between ZIF8/67–1/1 and $CuCo_2S_4$ [67]. The above results show that the interface of

CCS@ZIF8/67–1/1 heterojunction generates a local internal electric field due to electron transfer dynamics. The built-in electric field promotes better separation of the light-producing electrons and holes [68].

Based on the above characterization and corresponding analysis, the possible mechanism of the photocatalytic reaction of C-F@CCS@ZIF8/67–1/1 was proposed and detailed in Scheme 2. According to the previous calculation, the pre-contact band structures of ZIF8, ZIF8/67–2/1, ZIF8/67–1/1, ZIF8/67–1/2, ZIF67 and $CuCo_2S_4$ are summarized (Scheme 2a). Because ZIF8/67–1/1 is an n-type semiconductor, while $CuCo_2S_4$ is a p-type semiconductor. The Ef of ZIF8/67–1/1 and $CuCo_2S_4$ are located closer to the LUMO and VB, respectively. Therefore, when ZIF8/67–1/1 and $CuCo_2S_4$ semiconductors come into contact, the negative charge starts to migrate from ZIF8/67–1/1 to $CuCo_2S_4$ until the two semiconductors reach the same Ef value. Thus, the ZIF8/67–1/1 side has a positive interface charge, while the $CuCo_2S_4$ side has a negative interface charge. The built-in electric field (BIEF) from ZIF8/67–1/1 to $CuCo_2S_4$ is formed at the interface. Due to charge redistribution, the space charge region forms a ZIF8/67–1/1/ $CuCo_2S_4$ interface
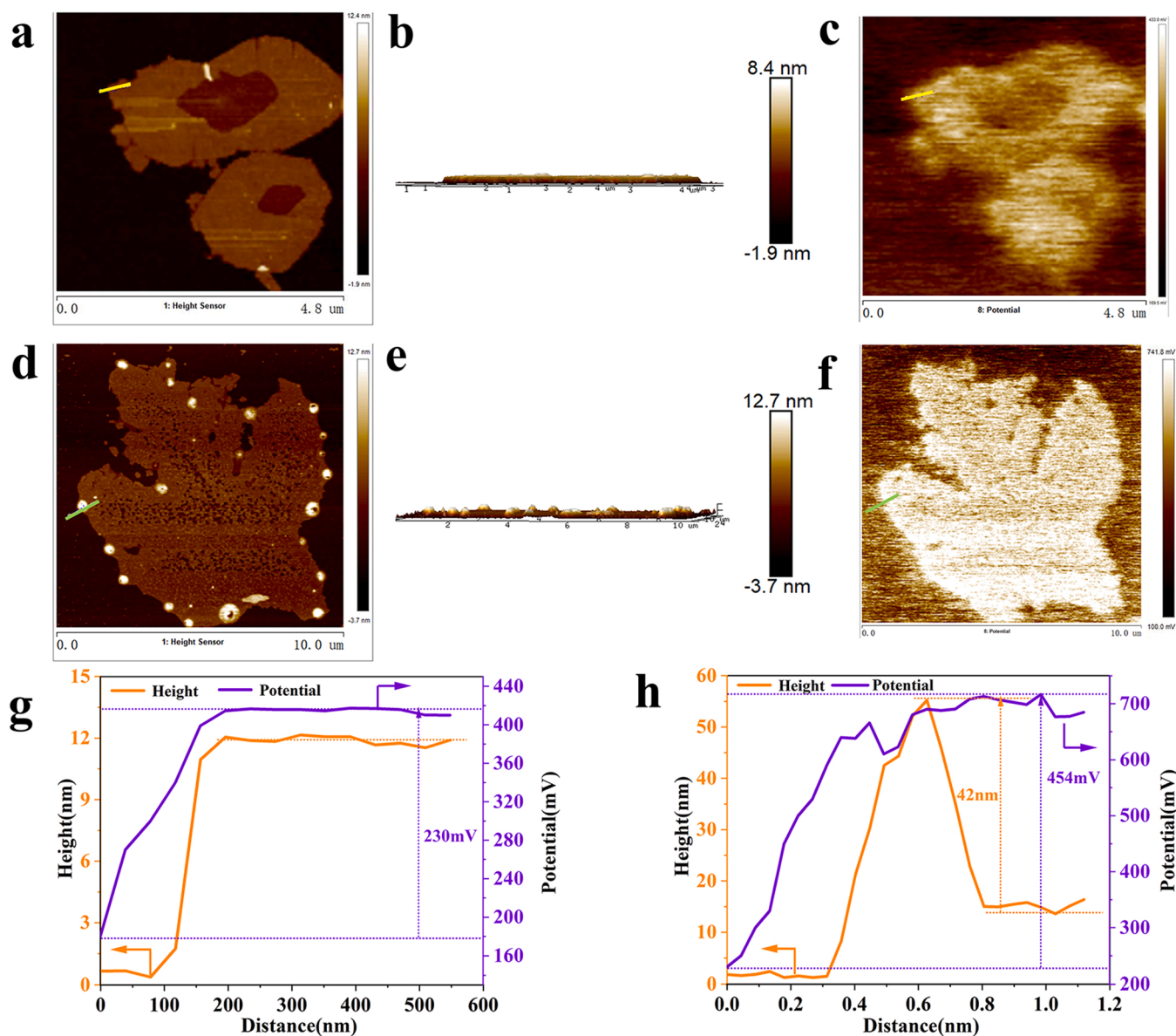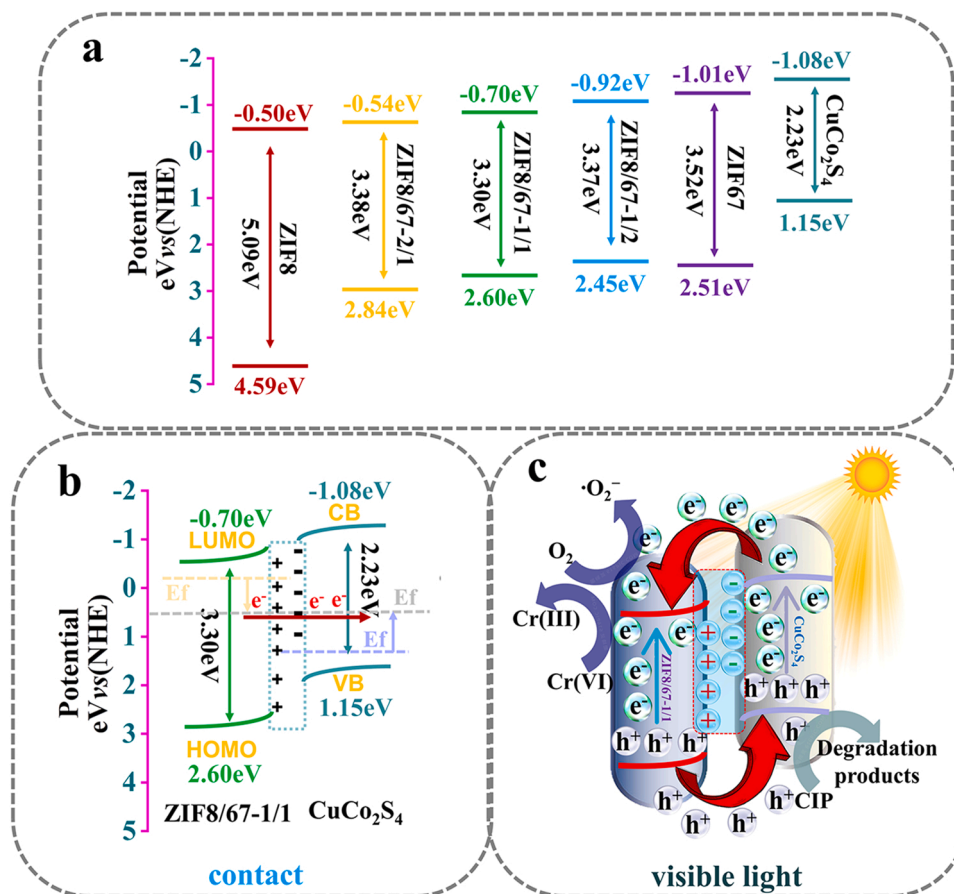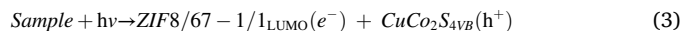

Fig. 10. (a) KPFM morphology, (b) 3D morphology map and (c) KPFM potential map of C-F@$CuCo_2S_4$ samples; (d) KPFM morphology, (e) 3D morphology diagram and (f) KPFM potential diagram of C-F@CCS@ZIF8/67–1/1 sample; The height curves (orange lines) and surface potentials (purple lines) corresponding to (g) C-F@$CuCo_2S_4$ and (h) C-F@CCS@ZIF8/67–1/1.

Scheme 2. Schematic illustration of photocatalytic mechanism for C-F@CCS@ZIF8/67–1/1 p-n heterojunction: (a) band structure of various catalysts, (b) internal electric fields and band edge bending of CuCo$_2$S$_4$ and ZIF8/67–1/1 after interfacial contact, and (c) charge transfer mechanism between CuCo$_2$S$_4$ and ZIF8/67–1/1 after light exposure.

with a strong internal electric field, and the ZIF8/67–1/1 band bends upward and the CuCo$_2$S$_4$ band bends downward, respectively, causing photogenerated carrier to drift until thermal equilibrium is reached (Scheme 2b) [69]. Under visible light or simulated sunlight, photogenerated electrons are excited from the HOMO orbital of ZIF8/67–1/1 to the LUMO orbital, and the photogenerated electrons of CuCo$_2$S$_4$ are excited from VB to the corresponding CB. Driven by a built-in electric field, electrons on the CuCo$_2$S$_4$ CB quickly transfer to the LUMO orbital of ZIF8/67–1/1, and holes on the HOMO orbital of ZIF8/67–1/1 transfer to the VB of CuCo$_2$S$_4$. Therefore, the spatial separation rate of hole-electron pairs is significantly improved, and ZIF8/67–1/1 and CuCo$_2$S$_4$ form p-n heterojunction with high photocatalytic activity (Scheme 2c) [70].

In the p-n heterostructure formed by C-F@CCS@ZIF8/67–1/1, the photogenerated electrons of ZIF8/67–1/1 in the LUMO orbit can be captured by O$_2$, resulting in the formation of •O^{2-}, because the LUMO potential of ZIF8/67–1/1 (−0.70 eV vs. NHE)) is more negative than O$_2$/•O^{2-} potential (−0.33 eV vs. NHE). Moreover, the LUMO potential of ZIF8/67–1/1 in the photocatalytic reduction of Cr(VI) is more negative than the standard reduction potential of Cr(VI)/Cr(III) (1.33 eV vs. NHE), indicating that the photocatalytic reduction of Cr(VI) is thermodynamically permissible [71]. Although the holes generated in the VB of CuCo$_2$S$_4$ cannot react with OH$^-$ to form •OH because the VB potential of CuCo$_2$S$_4$ (1.15 eV vs. NHE) is more negative than the OH$^-$/•OH potential (1.99 eV vs. NHE), they can be directly involved in the reaction with CIP for degradation purposes [72]. According to the above analysis, the corresponding photocatalytic reaction can be expressed by the following Eqs. (3) - (6).

$$Sample + h\nu \rightarrow ZIF8/67 - 1/1_{LUMO}(e^-) \ + \ CuCo_2S_{4VB}(h^+) \tag{3}$$

$$O_2 + e^- \rightarrow \cdot O_2 \tag{4}$$

$$\cdot O_2/h^+ + CIP \rightarrow degraded products \tag{5}$$

$$Cr(VI) + e^- \rightarrow Cr(III) \tag{6}$$

Thus, the interfacial enhancement p-n heterostructure scheme improves the lifetime of photogenerated carriers. In addition, C-F@CCS@ZIF8/67–1/1 can accelerate the enrichment of pollutants and provide numerous active sites due to its micro-mesoporous structure and large specific surface area. Moreover, this unique three-dimensional network structure can reduce charge transfer impedance and accelerate electron transfer, which is also conducive to improving photocatalytic performance.

3.4. CIP degradation pathways and toxicity

The intermediate product of the CIP degradation process was analyzed by the LC-MS method. The information of 10 intermediates was determined by mass spectrometry (Fig. S15 and Table S2). We predicted the possible degradation path of CIP based on the degradation intermediate product information (Fig. 11a). In pathway I, piperazinyl of CIP (*m/z* 332) is first oxidized to form P1 (*m/z* 362) under the joint action of •O^{2-} and h$^+$ [73]. Then h$^+$ continues to attack the piperazine ring causing the N-C bond to break to form P2 (*m/z* 334) and P3 (*m/z* 306) [74]. Then the N-C bond will continue to break to form P4 (*m/z* 263) under additional attack from h$^+$. In the subsequent reaction, P4
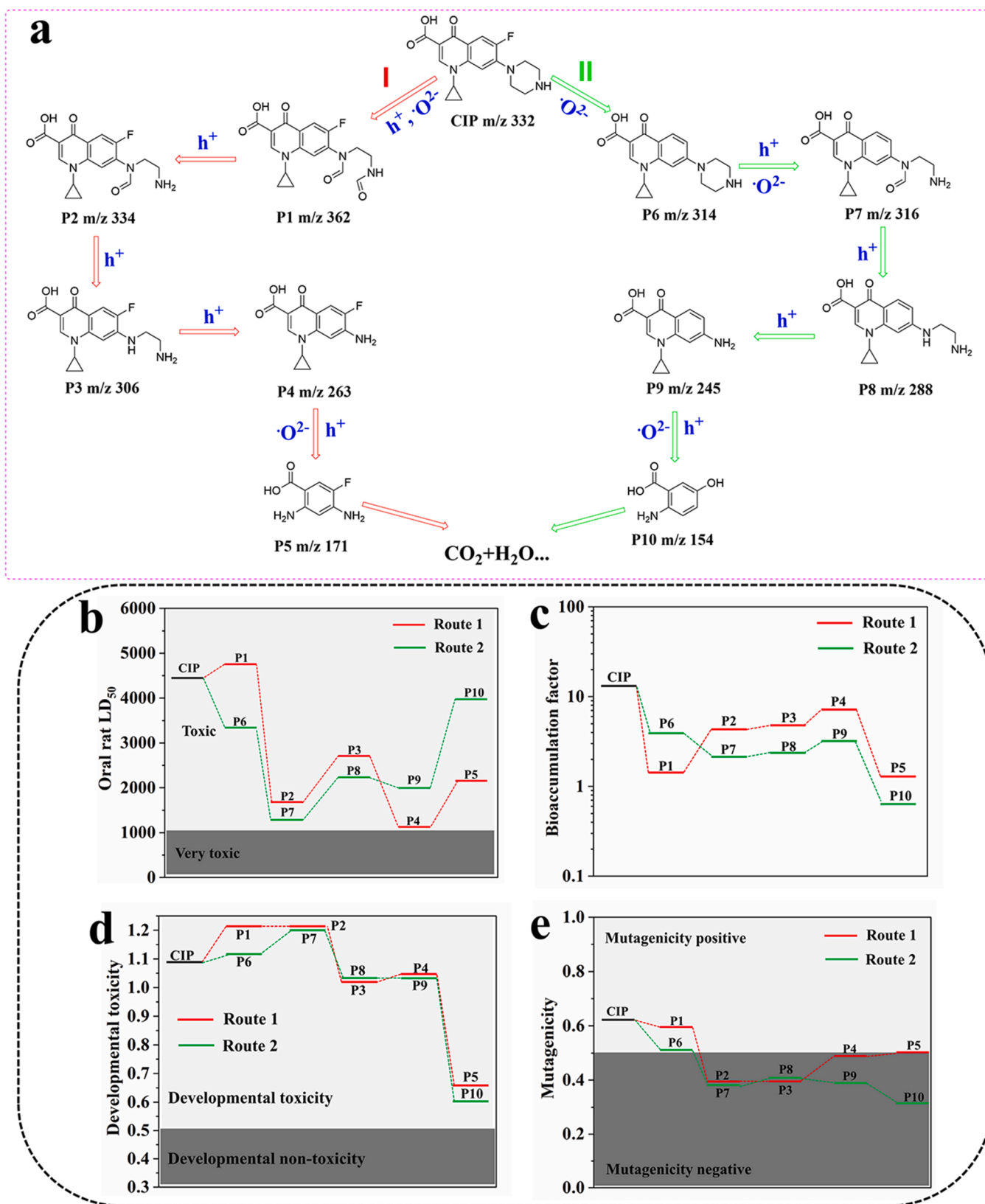
Fig. 11. (a) Possible pathways of C-F@CCS@ZIF8/67–1/1 photocatalytic degradation of CIP; QSAR analysis based on (b) Oral rat LD50, (c) Bioaccumulation factors, (d) Developmental toxicity, and (e) Mutagenicity.

was attacked by $\bullet O^{2-}$ and h^+, which further decomposed into P5 (m/z 171). The final mineralization forms water and carbon dioxide. In pathway II, CIP molecules are defluorinated and then oxidized. First, F is replaced by $\bullet O^{2-}$ attack to form P6 (m/z 314), then further oxidizes and destroys piperazine rings to form P7 (m/z 316) under the action of $\bullet O^{2-}$ and h^+ [75]. Immediately after under the action of h^+, N-C bonds continue to break to form P8 (m/z 288) and P9 (m/z 245). P9 undergoes oxidative decarboxylation to form P10 (m/z 154), which continues to decompose into water and carbon dioxide. This degradation path demonstrates the long-term performance of C-F@CCS@ZIF8/67–1/1 in dealing with CIP removal and mineralization.

To reveal whether CIP and its by-products pose a threat to the ecosystem, we used the toxicity estimation software tool (T.E.S.T) to predict oral rat LD50, bioaccumulation factors, developmental toxicity, and mutagenicity by quantitative structure activity relationship (QSAR). As can be seen from Fig. 11b, CIP in rats with an LD50 of 4344.04 mg/L orally was considered "toxic", and LD50 in most of the intermediates was reduced orally, indicating that the toxicity of the intermediates was not reduced [76]. As shown in Fig. 11c, after the initial attack and after further oxidation, the bioaccumulation factor of the intermediate was lower than CIP, indicating that the bioaccumulation decreased after degradation [77]. It can be seen from Fig. 11d that the developmental toxicity of intermediates except P1, P2, P6 and P7 is greater than that of CIP, and the developmental toxicity of other intermediates is also significantly reduced, which means that the toxicity is reduced. Moreover, mutagenicity results in the reduction of all intermediates, and most intermediates exhibit non-mutagenicity (Fig. 11e) [78]. Based on the above findings, although there are still a few byproducts with toxicity, compared with CIP, the overall biological toxicity is reduced, indicating that C-F@CCS@ZIF8/67–1/1 photocatalytic degradation of CIP is an environmental protection technology [79]. As shown in Fig. S16, the TOC removal rate of C-F@CCS@ZIF8/67–1/1 within 90 min is 56.8%, indicating that CIP can be partially mineralized into carbon dioxide and water. These results further indicate that photocatalyst C-F@CCS@ZIF8/67–1/1 can produce efficient free radicals to degrade CIP under visible light conditions, and can effectively reduce the toxicity and TOC residual rate of CIP in water.

3.5. Practical application of C-F@CCS@ZIF8/67–1/1

In this study, 1 M hydrochloric acid or 1 M sodium hydroxide was used to adjust pH, and the effects of different pH values on CIP degradation and Cr(VI) reduction efficiency were analyzed (Fig. 12a). The results show that when the pH value was 3, the removal efficiency of the two pollutants was the lowest, which was 71.1% and 71.7% respectively. This may be due to the easy decomposition of ZIF8/67 under acidic conditions. When the pH value is 7, the maximum degradation efficiency of CIP is 97.2%, which may be because the adsorption performance of CIP depends on the surface charge of the catalyst. CIP is known to have two different protonation pH values ($pK_{a1} = 6.14 \pm 0.13$, and $pK_{a2} = 8.70 \pm 0.09$) [80]. The zero-charge point (pzc) of C-F@CCS@ZIF8/67–1/1 is 7.14 at pH value (Fig. S17). Therefore, the surface of C-F@CCS@ZIF8/67–1/1 is positively charged at pH < 7.14 and negatively charged at pH > 7.14. In these two pH ranges, electrostatic repulsion prevents the photocatalyst from high CIP adsorption, leading to a decrease in degradation efficiency. Cr(VI) has different complexation forms under different pH conditions. Cr(VI) exists in the form of CrO_4^{2-} under acidic conditions and $HCrO_4^-$ under alkaline conditions. Under acidic conditions, excess hydrogen ion (H^+) is conducive to the reduction of $HCrO_4^-$ ion, and the corresponding reaction process (Eq. (7)). However, under alkaline conditions, the abundant hydroxide ions (OH^-) make the reduction process of the CrO_4^{2-} ion difficult to proceed smoothly (Eq. (8)) [81].

$$HCrO_4^- + 7H^+ + 3e^- \rightarrow Cr^{3+} + 4H_2O \tag{7}$$

$$CrO_4^- + 4H_2O + 4e^- \rightarrow Cr(OH)_3 + 5OH^- \tag{8}$$
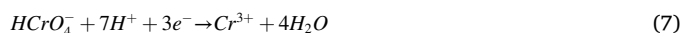
Under alkaline conditions, Cr(III) generated from Cr(VI) can form Cr(OH)$_3$, which will cover the active site on the catalyst surface and also reduce CIP degradation efficiency. In conclusion, the synergistic reduction efficiency of Cr(VI) can be significantly improved under acidic conditions. However, under neutral conditions, it is more conducive to CIP collaborative degradation. For cost and operational reasons, a condition with a pH of 7 was chosen as the initial condition.

Many organic matters are produced in the metabolic process of animals and plants, among which humic acid (HA) is a representative
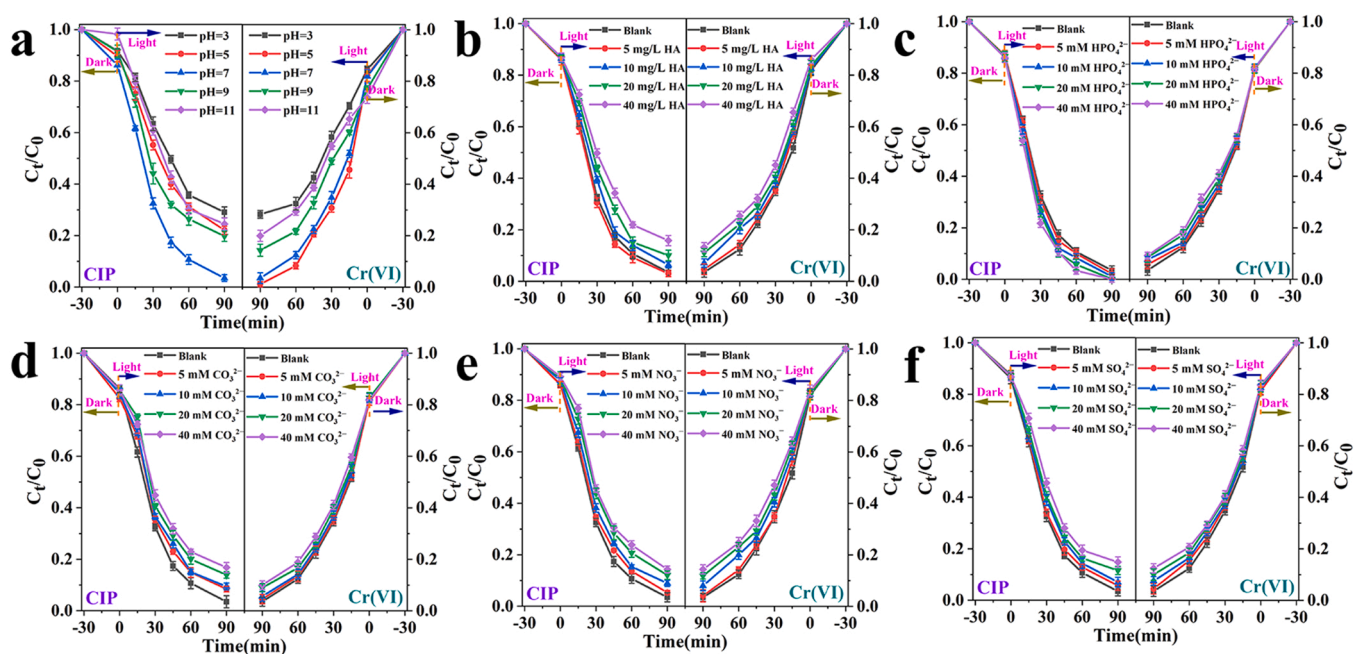

Fig. 12. Effects of (a) pH, (b) HA, (c) HPO_4^{2-}, (d) CO_3^{2-}, (e) NO_3^- and (f) SO_4^{2-} on the photocatalytic activity of C-F@CCS@ZIF8/67–1/1 under the coexistence of CIP and Cr(VI).

macromolecular organic matter and widely exists in water. As shown in Fig. 12b, when the concentration of HA changes from 0 to 5 mg/L, the removal efficiency of CIP is slightly improved, mainly because HA is a photosensitizer and can form $^3HA^*$ free radicals under low concentration conditions and participate in the degradation of CIP. However, when HA concentration increases, HA will react with free radicals and crowd out active sites to reduce photocatalytic efficiency. Since inorganic anions and cations (NO_3^-, SO_4^{2-}, HPO_4^{2-} and CO_3^{2-}) are commonly found in sewage and real water bodies, it is necessary to comprehensively study their effects on photocatalytic performance under their present conditions. Using 1 M initial salt solution, these different ions were adjusted to concentrations of 5 mM, 10 mM, 20 mM, and 40 mM in the simulated contamination solution. As shown in Fig. 12c, in the presence of HPO_4^{2-}, the higher the concentration of anions, the higher the CIP removal efficiency. The difference was that different amounts of NO_3^-, SO_4^{2-} and CO_3^{2-} inhibited the photocatalytic degradation of CIP significantly (Fig. 12d-f). The reason for this phenomenon may be that these ions react with free radicals to form active species with different catalytic activities [82]. The presence of anions in the reaction mixture also slightly hinders the Cr(VI) reduction reaction, probably due to the competitive effect between the adsorption of these anions and Cr(VI) on the catalyst surface [83]. In order to better evaluate the suitability of C-F@CCS@ZIF8/67–1/1 photocatalysis under environmental conditions, we studied the removal of CIP and Cr(VI) in different light conditions and different water substrates. The degradation efficiencies of

CIP in deionized water, tap water and river water were 97.2%, 87.1% and 80.1%, respectively, and the reduction efficiencies of Cr(VI) were 96.5%, 89.6% and 82.5%, respectively (Fig. S18a). Compared with deionized water, the removal efficiency of CIP and Cr(VI) is inhibited in environmental water bodies, especially in river water, due to the shielding effect caused by organic matter and the competition effect of inorganic matter. In order to verify the photocatalytic performance under real sunlight, we used an AM 1.5 G filter to provide simulated sunlight. Under simulated natural sunlight, the photocatalytic performance of C-F@CCS@ZIF8/67–1/1 in deionized water is even slightly better than that under visible light conditions (Fig. S18b). The superior photocatalytic effect may be caused by unfiltered UV light and thermal effects [84]. These results indicate that C-F@CCS@ZIF8/67–1/1 has the potential to be used in real water pollution treatment.

In order to verify the stability and reusability of C-F@CCS@ZIF8/67–1/1, 10 cycles of experiments were performed. Since the active component is grown in situ on the C-F surface, no complex recovery process is required (traditional recovery methods include centrifugal recovery, filter recovery and magnetic recovery, which are long and prone to secondary contamination), and only C-F@CCS@ZIF8/67–1/1 is simply clamped out of the post-reaction solution and washed with deionized water for the next experiment. In Fig. 13a, after 10 cycles, the degradation efficiency of CIP was reduced to 80.7% and the reduction efficiency of Cr(VI) was reduced to 80.3%. These results support the stability and reusability of C-F@CCS@ZIF8/67–1/1. It should be
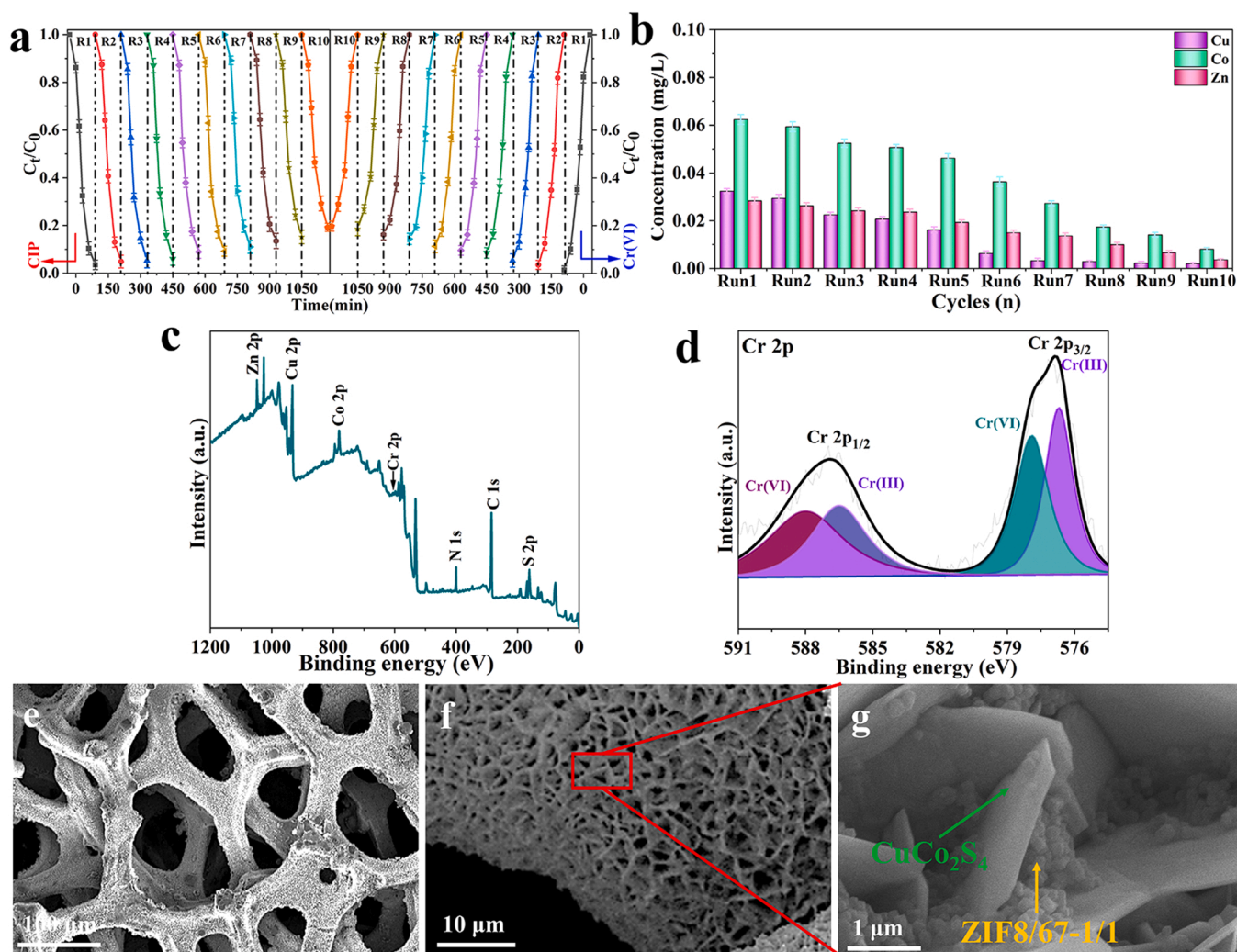

Fig. 13. (a) Cyclic tests on CIP degradation and Cr(VI) reduction of C-F@CCS@ZIF8/67–1/1 catalyst in coexisting environment; (b) Metal leaching tests during the cycle; (c) The XPS measured spectrum of C-F@CCS@ZIF8/67–1/1 and (d) the high-resolution spectrum of Cr 2p after the cycle; (e-g) SEM image after the cycle.

emphasized that the amount of metal ions leached after each cycle in this study is greatly lower than the amount of Cu (1.3 mg/L) and Zn (5.0 mg/L) in the U.S. Environmental Protection Agency (EPA) standards for drinking water (Fig. 13b). The amount of Co leached was also below the maximum allowable concentration of 0.2 mg/L for irrigation water in the United States. This result further demonstrates the safety of C-F@CCS@ZIF8/67–1/1 in the use process. In addition, we tested the XPS of the catalyst after cycling, and Fig. 13c show the presence of Cr on the surface of the photocatalyst after the reaction. The Cr 2p XPS spectrum in Fig. 13d reflects the characteristic peaks of Cr(III), whose binding energies are 576.7 and 586.5 eV, corresponding to Cr $2p_{3/2}$ and Cr $2p_{1/2}$, respectively, indicating the conversion of Cr(VI) to Cr(III) [85]. This suggests that minor inactivation is mainly related to the occupation of active sites by adsorbed degradation products. Nanoscale/microscale heterogeneous catalysts commonly have agglomeration and stability problems during use. As shown in Fig. 13e-g, SEM images of C-F@CCS@ZIF8/67–1/1 after the photocatalytic reaction were also similar to those before the reaction. The results show that $CuCo_2S_4$ with a vertical nanosheet structure can effectively avoid the aggregation of nanocatalysts during multiple uses. We compared various photocatalysts for simultaneous photocatalytic removal of organic pollutants and Cr(VI) to demonstrate the effectiveness of our multi-level photocatalysts, as shown in Table S3. The results show that the multi-level materials and porous materials photocatalyst has higher catalytic efficiency, and its recovery, stability and long-term service performance are much better than other reported photocatalyst materials due to the active component growing in situ on the recyclable substrate. The reasons for the excellent photocatalytic performance of C-F@CCS@ZIF8/67–1/1 multi-level photocatalyst prepared by us include the following: 1) $CuCo_2S_4$ has a vertical interconnected network structure, and C-F@CCS@ZIF8/67–1/1 has a high specific surface area and micro-nano pore structure, which not only improves the light capture and adsorption efficiency of reactants, but also promotes the transport of guest species to the binding site [86]. 2) Two-dimensional nanosheets formed by $CuCo_2S_4$ expose more active sites, and ZIF8/67–1/1 grows uniformly on the surface, avoiding agglomeration covering the active sites and improving the photocatalytic performance. 3) Traditional photocatalysts developed on recyclable substrates require the addition of adhesives to prevent the nanosheet from falling off (such as naphthol, which increases contact and transfer resistance). And this unique multi-level structure is different from traditional powder materials, which can be easily recycled after use without secondary pollution.

4. Conclusions

In summary, we constructed a new type of three-dimensional vertical $CuCo_2S_4$ nanosheet on the surface of C-F and anchored ZIF8/67–1/1 nanoparticles on the surface to form a p-n heterostructure. Under visible light or simulated sunlight, C-F@CCS@ZIF8/67–1/1 photocatalyst can synchronously remove CIP and Cr(VI) and is better than other composite catalysts. Experiments and DFT calculations show that the band gap decreases after the formation of the heterojunction, and the levels near the Fermi level are gradually distributed continuously, which increases the electrical conductivity and reactivity of the interface. And the electron orbitals have been redistributed to increase the ability to transfer electrons. Moreover, we determined the presence of the internal electric field by KPFM analysis. This interface enhancement effect promotes the separation of photogenerated carriers and greatly improves photocatalytic performance. The abundant oxygen vacancy on the surface, micro-mesoporous dispersed pores, large specific surface area and uniformly dispersed structure also accelerate the enrichment of pollutants and the separation of photogenic carriers. In addition, C-F@CCS@ZIF8/67–1/1 does not require complex recovery processes (traditional magnetic recovery, centrifugal recovery and filtration recovery), its structure and composition remain unchanged after 10 consecutive photocatalytic reactions, and the leaching concentration of

metal ions in the treated water is lower than permitted drinking water standards. The findings of this study provide a reliable method for the synthesis of metal foam-based photocatalysts and broaden the application of metal foams in environmental remediation.

CRediT authorship contribution statement

Jiliang Niu contributed to the conception of the study, **Ruixiang Hu** performed the experiment, **Liwen Tang** contributed significantly to analysis and manuscript preparation, **Yuxin Huang** participated in the mechanism analysis, **Jianhua Cheng** performed the data analyses and wrote the manuscript, **Yongyou Hu** helped perform the analysis with constructive discussions.

Declaration of Competing Interest

The authors declare that they have no known competing financial interests or personal relationships that could have appeared to influence the work reported in this paper.

Data Availability

No data was used for the research described in the article.

Appendix A. Supporting information

Supplementary data associated with this article can be found in the online version at doi:10.1016/j.apcatb.2023.122857.

References

[1] Y. Zhang, J. Xu, J. Zhou, L. Wang, Metal-organic framework-derived multifunctional photocatalysts, Chin. J. Catal. 43 (4) (2022) 971–1000, https://doi.org/10.1016/s1872-2067(21)63934-7.

[2] Z.-H. Diao, X.-R. Xu, D. Jiang, J.-J. Liu, L.-J. Kong, G. Li, L.-Z. Zuo, Q.-H. Wu, Simultaneous photocatalytic Cr(VI) reduction and ciprofloxacin oxidation over TiO 2 /Fe 0 composite under aerobic conditions: Performance, durability, pathway and mechanism, Chem. Eng. J. 315 (2017) 167–176, https://doi.org/10.1016/j.cej.2017.01.006.

[3] Y.-X. Li, Y.-C. Han, C.-C. Wang, Fabrication strategies and Cr(VI) elimination activities of the MOF-derivatives and their composites, Chem. Eng. J. 405 (2021), https://doi.org/10.1016/j.cej.2020.126648.

[4] C. Liu, X. Cui, Y. Li, Q. Duan, A hybrid hollow spheres Cu2O@TiO2-g-ZnTAPc with spatially separated structure as an efficient and energy-saving day-night photocatalyst for Cr(VI) reduction and organic pollutants removal, Chem. Eng. J. 399 (2020), https://doi.org/10.1016/j.cej.2020.125807.

[5] J. Ding, Y. Tang, S. Zheng, S. Zhang, H. Xue, Q. Kong, H. Pang, The synthesis of MOF derived carbon and its application in water treatment, Nano Res. 15 (8) (2022) 6793–6818, https://doi.org/10.1007/s12274-022-4327-1.

[6] Z.-H. Xie, H.-Y. Zhou, C.-S. He, Z.-C. Pan, G. Yao, B. Lai, Synthesis, application and catalytic performance of layered double hydroxide based catalysts in advanced oxidation processes for wastewater decontamination: A review, Chem. Eng. J. 414 (2021), https://doi.org/10.1016/j.cej.2021.128713.

[7] A. Meng, L. Zhang, B. Cheng, J. Yu, Dual cocatalysts in TiO(2) photocatalysis, Adv. Mater. 31 (30) (2019), e1807660, https://doi.org/10.1002/adma.201807660.

[8] J. Fu, J. Yu, C. Jiang, B. Cheng, g-C3N4-based heterostructured photocatalysts, Adv. Energy Mater. 8 (3) (2018), https://doi.org/10.1002/aenm.201701503.

[9] N.A. Nordin, M.A. Mohamed, M.N.I. Salehmin, S.F.Mohd Yusoff, Photocatalytic active metal–organic framework and its derivatives for solar-driven environmental remediation and renewable energy, Coord. Chem. Rev. 468 (2022), https://doi.org/10.1016/j.ccr.2022.214639.

[10] W. He, L. Liu, T. Ma, H. Han, J. Zhu, Y. Liu, Z. Fang, Z. Yang, K. Guo, Controllable morphology CoFe2O4/g-C3N4 p-n heterojunction photocatalysts with built-in electric field enhance photocatalytic performance, Appl. Catal. B: Environ. 306 (2022), https://doi.org/10.1016/j.apcatb.2022.121107.

[11] L. Sun, Y. Feng, K. Ma, X. Jiang, Z. Gao, J. Wang, N. Jiang, X. Liu, Synergistic effect of single-atom Ag and hierarchical tremella-like g-C3N4: Electronic structure regulation and multi-channel carriers transport for boosting photocatalytic

performance, Appl. Catal. B Environ. 306 (2022), https://doi.org/10.1016/j.apcatb.2022.121106.

[12] Y. Yang, C. Zhang, D. Huang, G. Zeng, J. Huang, C. Lai, C. Zhou, W. Wang, H. Guo, W. Xue, R. Deng, M. Cheng, W. Xiong, Boron nitride quantum dots decorated ultrathin porous g-C3N4: Intensified exciton dissociation and charge transfer for promoting visible-light-driven molecular oxygen activation, Appl. Catal. B: Environ. 245 (2019) 87–99, https://doi.org/10.1016/j.apcatb.2018.12.049.

[13] L. Zhang, J. Zhang, H. Yu, J. Yu, Emerging S-scheme photocatalyst, Adv. Mater. 34 (11) (2022), e2107668, https://doi.org/10.1002/adma.202107668.

[14] Y. Xia, J. Yu, Reaction: rational design of highly active photocatalysts for CO2 Conversion, Chem 6 (5) (2020) 1039–1040, https://doi.org/10.1016/j.chempr.2020.02.015.

[15] J. Zhang, W. Zhao, Z. Li, G. Lu, M. Zhu, Visible-light-assisted peroxymonosulfate activation over Fe(II)/V(IV) self-doped FeVO4 nanobelts with enhanced sulfamethoxazole degradation: Performance and mechanism, Chem. Eng. J. 403 (2021), https://doi.org/10.1016/j.cej.2020.126384.

[16] L. Meng, C. Zhao, T. Wang, H. Chu, C.-C. Wang, Efficient ciprofloxacin removal over Z-scheme ZIF-67/V-BiOIO3 heterojunctions: Insight into synergistic effect between adsorption and photocatalysis, Sep. Purif. Technol. 313 (2023), https://doi.org/10.1016/j.seppur.2023.123511.

[17] J. Li, H. Wang, Z. Qi, C. Ma, Z. Zhang, B. Zhao, L. Wang, H. Zhang, Y. Chong, X. Chen, X. Cheng, D.D. Dionysiou, Kinetics and mechanisms of electrocatalytic hydrodechlorination of diclofenac on Pd-Ni/PPy-rGO/Ni electrodes, Appl. Catal. B Environ. 268 (2020), https://doi.org/10.1016/j.apcatb.2020.118696.

[18] J. Guo, L. Jiang, J. Liang, W. Xu, H. Yu, J. Zhang, S. Ye, W. Xing, X. Yuan, Photocatalytic degradation of tetracycline antibiotics using delafossite silver ferrite-based Z-scheme photocatalyst: Pathways and mechanism insight, Chemosphere 270 (2021), 128651, https://doi.org/10.1016/j.chemosphere.2020.128651.

[19] X.-W. Zhang, M.-Y. Lan, F. Wang, X.-H. Yi, C.-C. Wang, ZIF-67-based catalysts in persulfate advanced oxidation processes (PS-AOPs) for water remediation, J. Environ. Chem. Eng. 10 (3) (2022), https://doi.org/10.1016/j.jece.2022.107997.

[20] Y. Cao, M.A. El-Shorbagy, K. Sharma, S. Alamri, A.A. Rajhi, A.E. Anqi, A.A. Aly, B. F. Felemban, In-situ synthesis of a novel ZnO/CuCo2S4 p-n heterojunction photocatalyst with improved phenol and rhodamine B degradation performance and investigating the mechanism of charge carrier separation, J. Photochem. Photobiol. A: Chem. 425 (2022), https://doi.org/10.1016/j.jphotochem.2021.113676.

[21] J. Liu, R. Li, X. Zu, X. Zhang, Y. Wang, Y. Wang, C. Fan, Photocatalytic conversion of nitrogen to ammonia with water on triphase interfaces of hydrophilic-hydrophobic composite Bi4O5Br2/ZIF-8, Chem. Eng. J. 371 (2019) 796–803, https://doi.org/10.1016/j.cej.2019.03.283.

[22] W. Fei, J. Gao, N. Li, D. Chen, Q. Xu, H. Li, J. He, J. Lu, A visible-light active p-n heterojunction NiFe-LDH/Co(3)O(4) supported on Ni foam as photoanode for photoelectrocatalytic removal of contaminants, J. Hazard Mater. 402 (2021), 123515, https://doi.org/10.1016/j.jhazmat.2020.123515.

[23] F. Deng, S. Li, M. Zhou, Y. Zhu, S. Qiu, K. Li, F. Ma, J. Jiang, A biochar modified nickel-foam cathode with iron-foam catalyst in electro-Fenton for sulfamerazine degradation, Appl. Catal. B: Environ. 256 (2019), https://doi.org/10.1016/j.apcatb.2019.117796.

[24] F. Deng, H. Olvera-Vargas, O. Garcia-Rodriguez, S. Qiu, F. Ma, Z. Chen, O. Lefebvre, Unconventional electro-Fenton process operating at a wide pH range with Ni foam cathode and tripolyphosphate electrolyte, J. Hazard Mater. 396 (2020), 122641, https://doi.org/10.1016/j.jhazmat.2020.122641.

[25] S. Panneri, M. Thomas, P. Ganguly, B.N. Nair, A.P. Mohamed, K.G.K. Warrier, U. S. Hareesh, C3N4 anchored ZIF 8 composites: photo-regenerable, high capacity sorbents as adsorptive photocatalysts for the effective removal of tetracycline from water, Catal. Sci. Technol. 7 (10) (2017) 2118–2128, https://doi.org/10.1039/c7cy00348j.

[26] J. Zhao, X. Quan, S. Chen, Y. Liu, H. Yu, Cobalt nanoparticles encapsulated in porous carbons derived from core-shell ZIF67@ZIF8 as efficient electrocatalysts for oxygen evolution reaction, ACS Appl. Mater. Interfaces 9 (34) (2017) 28685–28694, https://doi.org/10.1021/acsami.7b10138.

[27] S. Czioska, J Wang, X. Teng, Z. Chen, Hierarchically structured CuCo2S4 nanowire arrays as efficient bifunctional electrocatalyst for overall water splitting, ACS Sustain. Chem. Eng. 6 (9) (2018) 11877–11883, https://doi.org/10.1021/acssuschemeng.8b02155.

[28] Z. Sanaei, A. Shamsipur, B. Ramezanzadeh, Manipulating a smart multi-functional nano-carrier based on l-cysteine-GO-ZIF67@ZIF8 core@shell MOFs-LDH for designing an excellent self-healing coating, Appl. Mater. Today 30 (2023), https://doi.org/10.1016/j.apmt.2022.101718.

[29] M. Zhang, N. Fang, X. Song, Y. Chu, S. Shu, Y. Liu, p-n heterojunction photocatalyst Mn(0.5)Cd(0.5)S/CuCo(2)S(4) for highly efficient visible light-driven H(2) production, ACS Omega 5 (50) (2020) 32715–32723, https://doi.org/10.1021/acsomega.0c05106.

[30] J. Zhang, W. Geng, L. Shi, C. Yang, X. Zhang, Y. Geng, R. Arjan Kalyan Hirani, X. Xu, J. Wei, Y. Jing, S. Zhang, H. Zhang, S. Wang, H. Sun, One–pot synthesis of boron and nitrogen co–doped nanocarbons for efficient catalytic reduction of nitrophenols, Chem. Eng. J. 439 (2022), https://doi.org/10.1016/j.cej.2022.135733.

[31] K. Wang, N. Cai, F. Yu, M. Wang, Bead-like PCM composite network with reinforced heat storage performance for highly efficient battery cooling, J. Energy Storage 54 (2022), https://doi.org/10.1016/j.est.2022.105335.

[32] S. Ahn, K. Klyukin, R.J. Wakeham, J.A. Rudd, A.R. Lewis, S. Alexander, F. Carla, V. Alexandrov, E. Andreoli, Poly-amide modified copper foam electrodes for

enhanced electrochemical reduction of carbon dioxide, ACS Catal. 8 (5) (2018) 4132–4142, https://doi.org/10.1021/acscatal.7b04347.

[33] Y. Wang, F. Lin, J. Peng, Y. Dong, W. Li, Y. Huang, A robust bilayer nanofilm fabricated on copper foam for oil–water separation with improved performances, J. Mater. Chem. A 4 (26) (2016) 10294–10303, https://doi.org/10.1039/c6ta02021f.

[34] H. You, L. Zhang, Y. Jiang, T. Shao, M. Li, J. Gong, Bubble-supported engineering of hierarchical CuCo2S4 hollow spheres for enhanced electrochemical performance, J. Mater. Chem. A 6 (13) (2018) 5265–5270, https://doi.org/10.1039/c7ta07890k.

[35] Z. Wang, S. Chen, L. Wang, S. Gao, M. Li, H. Li, Y. Zhu, E. Shangguan, Microwave-anion-exchange route to spinel CuCo2S4 nanosheets as cathode materials for magnesium storage, J. Power Sources 556 (2023), https://doi.org/10.1016/j.jpowsour.2022.232480.

[36] H. Wang, X. Li, F. Su, J. Xie, Y. Xin, W. Zhang, C. Liu, D. Yao, Y. Zheng, Core-shell ZIF67@ZIF8 modified with phytic acid as an effective flame retardant for improving the fire safety of epoxy resins, ACS Omega 7 (25) (2022) 21664–21674, https://doi.org/10.1021/acsomega.2c01545.

[37] J. Lin, H. Jia, H. Liang, S. Chen, Y. Cai, J. Qi, C. Qu, J. Cao, W. Fei, J. Feng, Hierarchical CuCo2S4@NiMn-layered double hydroxide core-shell hybrid arrays as electrodes for supercapacitors, Chem. Eng. J. 336 (2018) 562–569, https://doi.org/10.1016/j.cej.2017.12.055.

[38] S. Xiao, D. Pan, R. Liang, W. Dai, Q. Zhang, G. Zhang, C. Su, H. Li, W. Chen, Bimetal MOF derived mesocrystal ZnCo2O4 on rGO with High performance in visible-light photocatalytic NO oxidization, Appl. Catal. B Environ. 236 (2018) 304–313, https://doi.org/10.1016/j.apcatb.2018.05.033.

[39] X. Yuan, S. Qu, X. Huang, X. Xue, C. Yuan, S. Wang, L. Wei, P. Cai, Design of core-shelled g-C3N4@ZIF-8 photocatalyst with enhanced tetracycline adsorption for boosting photocatalytic degradation, Chem. Eng. J. 416 (2021), https://doi.org/10.1016/j.cej.2021.129148.

[40] R. Yang, Z. Zhu, C. Hu, S. Zhong, L. Zhang, B. Liu, W. Wang, One-step preparation (3D/2D/2D) BiVO4/FeVO4/rGO heterojunction composite photocatalyst for the removal of tetracycline and hexavalent chromium ions in water, Chem. Eng. J. 390 (2020), https://doi.org/10.1016/j.cej.2020.124522.

[41] F. Zhao, Y. Wang, X. Zhang, Y. Liang, F. Zhang, Y. Wang, Y. Liu, H. Wang, Bi4O5Br2/ZIF-8, Chem. Eng. J. 371 (2019) 796–803, https://doi.org/10.1016/j.cej.2019.03.283. [text approximate]

[41] F. Deng, S. Hammouda, Y. Liu, X. Min, C.-J. Tang, M. Sillanpää, K. Sivula, S. Wang, MIL-101(Fe)/g-C3N4 for enhanced visible-light-driven photocatalysis toward simultaneous reduction of Cr(VI) and oxidation of bisphenol A in aqueous media, Appl. Catal. B Environ. 272 (2020), https://doi.org/10.1016/j.apcatb.2020.119033.

[42] X. Wei, Y. Wang, Y. Huang, C. Fan, Composite ZIF-8 with CQDs for boosting visible-light-driven photocatalytic removal of NO, J. Alloy. Compd. 802 (2019) 467–476, https://doi.org/10.1016/j.jallcom.2019.06.086.

[43] K. Shahzad, M.B. Tahir, M. Sagir, M.R. Kabli, Role of CuCo2S4 in Z-scheme MoSe2/BiVO4 composite for efficient photocatalytic reduction of heavy metals, Ceram. Int. 45 (17) (2019) 23225–23232, https://doi.org/10.1016/j.ceramint.2019.08.018.

[44] P. Lv, F. Duan, J. Sheng, S. Lu, H. Zhu, M. Du, M. Chen, The 2D/2D p–n heterojunction of ZnCoMOF/g-C3N4 with enhanced photocatalytic hydrogen evolution under visible light irradiation, Appl. Organomet. Chem. 35 (3) (2020), https://doi.org/10.1002/aoc.6124.

[45] Z. Yang, X. Xia, L. Shao, L. wang, Y. Liu, Efficient photocatalytic degradation of tetracycline under visible light by Z-scheme Ag3PO4/mixed-valence MIL-88A(Fe) heterojunctions: Mechanism insight, degradation pathways and DFT calculation, Chem. Eng. J. 410 (2021), https://doi.org/10.1016/j.cej.2021.128454.

[46] R.R. Nallapureddy, M.R. Pallavolu, J. Nallapureddy, A.K. Yedluri, S.W. Joo, Z-scheme photocatalysis and photoelectrochemical platform with a Co3O4-CuO heterogeneous catalyst for the removal of water pollutants and generation of energy, J. Clean. Prod. 382 (2023), https://doi.org/10.1016/j.jclepro.2022.135302.

[47] M. Chauhan, K. Soni, P.E. Karthik, K.P. Reddy, C.S. Gopinath, S. Deka, Promising visible-light driven hydrogen production from water on a highly efficient CuCo2S4 nanosheet photocatalyst, J. Mater. Chem. A 7 (12) (2019) 6985–6994, https://doi.org/10.1039/c9ta00391f.

[48] Y. Tang, X. Li, H. Zhang, T. Ouyang, Y. Jiang, M. Mu, X. Yin, Cobalt-based ZIF coordinated hybrids with defective TiO(2-x) for boosting visible light-driven photo-Fenton-like degradation of bisphenol A, Chemosphere 259 (2020), 127431, https://doi.org/10.1016/j.chemosphere.2020.127431.

[49] L. Zhang, G. Wang, X. Hao, Z. Jin, Y. Wang, MOFs-derived Cu3P/CoP p-n heterojunction for enhanced photocatalytic hydrogen evolution, Chem. Eng. J. 395 (2020), https://doi.org/10.1016/j.cej.2020.125113.

[50] B. Han, B. Zhu, Y. Liu, Q. Qiu, J. Li, T. Liang, T. Xie, Enhanced photocatalytic degradation activity via a stable perovskite-type LaFeO3/In2S3 Z-scheme heterostructured photocatalyst: Unobstructed photoexcited charge behavior of Z-scheme photocatalytic system exploration, J. Alloy. Compd. 901 (2022), https://doi.org/10.1016/j.jallcom.2022.163628.

[51] L. Bi, D. Meng, Q. Bu, Y. Lin, D. Wang, T. Xie, Electron acceptor of Ni decorated porous carbon nitride applied in photocatalytic hydrogen production, Phys. Chem. Chem. Phys. 18 (46) (2016) 31534–31541, https://doi.org/10.1039/c6cp05618k.

[52] J. Yu, X. Wang, L. Chen, G. Lu, G. Shi, X. Xie, Y. Wang, J. Sun, Enhanced adsorption and visible-light photocatalytic degradation of toluene by CQDs/UiO-66 MOG with hierarchical pores, Chem. Eng. J. 435 (2022), https://doi.org/10.1016/j.cej.2022.135033.

[53] Z. Zhai, K. Ren, X. Zheng, X. Chen, Y. Dong, H. Shi, Simultaneous photocatalytic tetracycline oxidation and chromate reduction via a jointed synchronous pathway upon Z-scheme Bi12O17Cl2/AgBr: insight into intermediates and mechanism, Environ. Sci. Nano 9 (5) (2022) 1780–1793, https://doi.org/10.1039/d2en00028h.

[54] L. Hou, W. Li, Z. Wu, Q. Wei, H. Yang, Y. Jiang, T. Wang, Y. Wang, Q. He, Embedding ZnCdS@ZnIn2S4 into thiazole-modified g-C3N4 by electrostatic self-assembly to build dual Z-scheme heterojunction with spatially separated active centers for photocatalytic H2 evolution and ofloxacin degradation, Sep. Purif. Technol. 290 (2022), https://doi.org/10.1016/j.seppur.2022.120858.

[55] F. Guo, W. Shi, H. Wang, M. Han, W. Guan, H. Huang, Y. Liu, Z. Kang, Study on highly enhanced photocatalytic tetracycline degradation of type II AgI/CuBi(2)O (4) and Z-scheme AgBr/CuBi(2)O(4) heterojunction photocatalysts, J. Hazard Mater. 349 (2018) 111–118, https://doi.org/10.1016/j.jhazmat.2018.01.042.

[56] J. Qiu, X.F. Zhang, X. Zhang, Y. Feng, Y. Li, L. Yang, H. Lu, J. Yao, Constructing Cd (0.5)Zn(0.5)S@ZIF-8 nanocomposites through self-assembly strategy to enhance Cr (VI) photocatalytic reduction, J. Hazard Mater. 349 (2018) 234–241, https://doi.org/10.1016/j.jhazmat.2018.02.009.

[57] W. Zhao, J. Qin, W. Teng, J. Mu, C. Chen, J. Ke, J.C. Huang, B. Liu, S. Wang, Catalytic photo-redox of simulated air into ammonia over bimetallic MOFs nanosheets with oxygen vacancies, Appl. Catal. B Environ. 305 (2022), https://doi.org/10.1016/j.apcatb.2021.121046.

[58] M. Chauhan, K.P. Reddy, C.S. Gopinath, S. Deka, Copper cobalt sulfide nanosheets realizing a promising electrocatalytic oxygen evolution reaction, ACS Catal. 7 (9) (2017) 5871–5879, https://doi.org/10.1021/acscatal.7b01831.

[59] S. Liu, L. Kang, J. Hu, E. Jung, J. Henzie, A. Alowasheeir, J. Zhang, L. Miao, Y. Yamauchi, S.C. Jun, Realizing superior redox kinetics of hollow bimetallic sulfide nanoarchitectures by defect-induced manipulation toward flexible solid-state supercapacitors, Small 18 (5) (2022), e2104507, https://doi.org/10.1002/smll.202104507.

[60] Y. Wang, L. Rao, P. Wang, Z. Shi, L. Zhang, Photocatalytic activity of N-TiO2/O-doped N vacancy of g-C3N4 and the intermediates toxicity evaluation under tetracycline hydrochloride and Cr(VI) coexistence environment, Appl. Catal. B Environ. 262 (2020), https://doi.org/10.1016/j.apcatb.2019.118308.

[61] T. Xu, R. Zou, X. Lei, X. Qi, Q. Wu, W. Yao, Q. Xu, New and stable g-C3N4/HAp composites as highly efficient photocatalysts for tetracycline fast degradation, Appl. Catal. B Environ. 245 (2019) 662–671, https://doi.org/10.1016/j.apcatb.2019.01.020.

[62] S. Gao, W. Cen, Q. Li, J. Li, Y. Lu, H. Wang, Z. Wu, A mild one-step method for enhancing optical absorption of amine-functionalized metal-organic frameworks, Appl. Catal. B Environ. 227 (2018) 190–197, https://doi.org/10.1016/j.apcatb.2018.01.007.

[63] Z. Yang, C. Chen, B. Li, Y. Zheng, X. Liu, J. Shen, Y. Zhang, S. Wu, A core–shell 2D-MoS2@MOF heterostructure for rapid therapy of bacteria-infected wounds by enhanced photocatalysis, Chem. Eng. J. 451 (2023), https://doi.org/10.1016/j.cej.2022.139127.

[64] K. Qi, Y. Ye, B. Wei, M. Li, Y. Lun, X. Xie, H. Xie, N-CQDs from reed straw enriching charge over BiO(2-x)/BiOCl p-n heterojunction for improved visible-light-driven photodegradation of organic pollutants, J. Hazard Mater. 432 (2022), 128759, https://doi.org/10.1016/j.jhazmat.2022.128759.

[65] L. Wang, G. Tang, S. Liu, H. Dong, Q. Liu, J. Sun, H. Tang, Interfacial active-site-rich 0D Co3O4/1D TiO2 p-n heterojunction for enhanced photocatalytic hydrogen evolution, Chem. Eng. J. 428 (2022), https://doi.org/10.1016/j.cej.2021.131338.

[66] P. Ju, L. Hao, Y. Zhang, J. Sun, K. Dou, Z. Lu, D. Liao, X. Zhai, C. Sun, In-situ topotactic construction of novel rod-like Bi2S3/Bi5O7I p-n heterojunctions with highly enhanced photocatalytic activities, J. Mater. Sci. Technol. 135 (2023) 126–141, https://doi.org/10.1016/j.jmst.2022.07.014.

[67] S. Gupta, D. Varandani, A.K. Sharma, V.R. Satsangi, B.R. Mehta, Nanoscale interface mapping of a CdS–CZTS single nanorod heterojunction using Kelvin probe force microscopy, Appl. Surf. Sci. 331 (2015) 327–332, https://doi.org/10.1016/j.apsusc.2015.01.092.

[68] M. Li, Y. Wang, N. Tian, H. Huang, Heterojunction and ferroelectric polarization co-promoting photocatalytic activity, Appl. Surf. Sci. 587 (2022), https://doi.org/10.1016/j.apsusc.2022.152852.

[69] C. Deng, F. Ye, T. Wang, X. Ling, L. Peng, H. Yu, K. Ding, H. Hu, Q. Dong, H. Le, Y. Han, Developing hierarchical CdS/NiO hollow heterogeneous architectures for boosting photocatalytic hydrogen generation, Nano Res. 15 (3) (2021) 2003–2012, https://doi.org/10.1007/s12274-021-3960-4.

[70] Y. Wang, C. Yang, K. Zhang, L. Guo, R. Li, A. Zaheer, F. Fu, B. Xu, D. Wang, In-Situ Construction of 2D/2D CuCo2S4/Bi2WO6 contact heterojunction as a visible-light-driven fenton-like catalyst with highly efficient charge transfer for highly efficient

degradation of tetracycline hydrochloride, Colloids Surf. A: Physicochem. Eng. Asp. 634 (2022), https://doi.org/10.1016/j.colsurfa.2021.127965.

[71] J. Zheng, Z. Lei, Incorporation of CoO nanoparticles in 3D marigold flower-like hierarchical architecture MnCo2O4 for highly boosting solar light photo-oxidation and reduction ability, Appl. Catal. B: Environ. 237 (2018) 1–8, https://doi.org/10.1016/j.apcatb.2018.05.060.

[72] Z. Zhang, J. Huang, Y. Fang, M. Zhang, K. Liu, B. Dong, A nonmetal plasmonic Z-scheme photocatalyst with UV- to NIR-driven photocatalytic protons reduction, Adv. Mater. 29 (18) (2017), https://doi.org/10.1002/adma.201606688.

[73] X. Hu, X. Hu, Q. Peng, L. Zhou, X. Tan, L. Jiang, C. Tang, H. Wang, S. Liu, Y. Wang, Z. Ning, Mechanisms underlying the photocatalytic degradation pathway of ciprofloxacin with heterogeneous TiO2, Chem. Eng. J. 380 (2020), https://doi.org/10.1016/j.cej.2019.122366.

[74] T. Ahamad, M. Naushad, S.M. Alshehri, Analysis of degradation pathways and intermediates products for ciprofloxacin using a highly porous photocatalyst, Chem. Eng. J. 417 (2021), https://doi.org/10.1016/j.cej.2020.127969.

[75] F. Guo, H. Zhang, H. Li, Z. Shen, Modulating the oxidative active species by regulating the valence of palladium cocatalyst in photocatalytic degradation of ciprofloxacin, Appl. Catal. B Environ. 306 (2022), https://doi.org/10.1016/j.apcatb.2022.121092.

[76] Q. Su, J. Li, B. Wang, Y. Li, La Hou, Direct Z-scheme Bi2MoO6/UiO-66-NH2 heterojunctions for enhanced photocatalytic degradation of ofloxacin and ciprofloxacin under visible light, Appl. Catal. B: Environ. 318 (2022), https://doi.org/10.1016/j.apcatb.2022.121820.

[77] F. Wang, S.S. Liu, Z. Feng, H. Fu, M. Wang, P. Wang, W. Liu, C.C. Wang, High-efficient peroxymonosulfate activation for rapid atrazine degradation by FeS(x)@MoS(2) derived from MIL-88A(Fe), J. Hazard Mater. 440 (2022), 129723, https://doi.org/10.1016/j.jhazmat.2022.129723.

[78] M. Cai, Y. Liu, C. Wang, W. Lin, S. Li, Novel Cd0.5Zn0.5S/Bi2MoO6 S-scheme heterojunction for boosting the photodegradation of antibiotic enrofloxacin: Degradation pathway, mechanism and toxicity assessment, Sep. Purif. Technol. 304 (2023), https://doi.org/10.1016/j.seppur.2022.122401.

[79] Q. Li, G. Wei, G. Duan, L. Zhang, Z. Li, Z. Wei, Q. Zhou, R. Pei, Photocatalysis activation of peroxydisulfate over oxygen vacancies-rich mixed metal oxide derived from red mud-based layered double hydroxide for ciprofloxacin degradation, Sep. Purif. Technol. 289 (2022), https://doi.org/10.1016/j.seppur.2022.120733.

[80] F. Du, Z. Lai, H. Tang, H. Wang, C. Zhao, Construction and application of BiOCl/Cu-doped Bi(2)S(3) composites for highly efficient photocatalytic degradation of ciprofloxacin, Chemosphere 287 (Pt 4) (2022), 132391, https://doi.org/10.1016/j.chemosphere.2021.132391.

[81] Y. Zhang, S.-J. Park, Facile construction of MoO3@ZIF-8 core-shell nanorods for efficient photoreduction of aqueous Cr (VI), Appl. Catal. B Environ. 240 (2019) 92–101, https://doi.org/10.1016/j.apcatb.2018.08.077.

[82] Q. Si, W. Guo, H. Wang, B. Liu, S. Zheng, Q. Zhao, H. Luo, N. Ren, T. Yu, Difunctional carbon quantum dots/g-C3N4 with in-plane electron buffer for intense tetracycline degradation under visible light: Tight adsorption and smooth electron transfer, Appl. Catal. B: Environ. 299 (2021), https://doi.org/10.1016/j.apcatb.2021.120694.

[83] M. Abinaya, K. Govindan, M. Kalpana, K. Saravanakumar, S.L. Prabavathi, V. Muthuraj, A. Jang, Reduction of hexavalent chromium and degradation of tetracycline using a novel indium-doped Mn(2)O(3) nanorod photocatalyst, J. Hazard Mater. 397 (2020), 122885, https://doi.org/10.1016/j.jhazmat.2020.122885.

[84] J. Guo, H. Sun, X. Yuan, L. Jiang, Z. Wu, H. Yu, N. Tang, M. Yu, M. Yan, J. Liang, Photocatalytic degradation of persistent organic pollutants by Co-Cl bond reinforced CoAl-LDH/Bi(12)O(17)Cl(2) photocatalyst: mechanism and application prospect evaluation, Water Res 219 (2022), 118558, https://doi.org/10.1016/j.watres.2022.118558.

[85] S. Chen, B. Li, D. Huang, P. Xu, Y. Chen, L. Lei, Z. Wang, R. Deng, L. Du, G. Wang, Jointed synchronous photocatalytic oxidation and chromate reduction enabled by the defect distribution upon BiVO(4): mechanism insight and toxicity assessment, ACS Appl. Mater. Interfaces 13 (15) (2021) 17586–17598, https://doi.org/10.1021/acsami.1c01998.

[86] X. Li, J. Yu, M. Jaroniec, Hierarchical photocatalysts, Chem. Soc. Rev. 45 (9) (2016) 2603–2636, https://doi.org/10.1039/c5cs00838g.